LUND UNIVERSITY

Development of photofragmentation-based diagnostics

Larsson, Kajsa

2018

[Link to publication](#)

Total number of authors:
1

Development of photofragmentation-based diagnostics

KAJSA LARSSON

DEPARTMENT OF PHYSICS | FACULTY OF ENGINEERING | LUND UNIVERSITY

Development of photofragmentation-based diagnostics

Kajsa Larsson
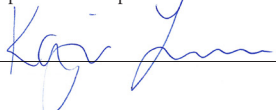

LUND
UNIVERSITY

DOCTORAL DISSERTATION
by due permission of the Faculty of Engineering, Lund University, Sweden.
To be defended at Rydbergsalen, Fysicum, Professorsgatan 1. 23rd February 2018 at 09.15.

Faculty opponent
Prof. Robert W. Pitz, Department of Mechanical Engineering, Vanderbilt University, Nashville, TN, USA

Organization LUND UNIVERSITY Division of Combustion Physics, Department of Physics P.O Box 118, SE-211 00 Lund, Sweden	Document name Doctoral Dissertation
	Date of issue: 2018-01-30
Author: Kajsa Larsson	CODEN: LUTFD2/TFCP-210-SE
	Sponsoring organization

Title: Development of Photofragmentation-Based Diagnostics

Abstract

Development of photofragmentation-based diagnostic concepts for studying H_2O_2, H_2O, HO_2 and O_3 in three different measurement environments, i.e. a flow of vaporized H_2O_2/H_2O, a premixed laminar methane/air flame and a plasma, produced by a gliding arc discharge, are reported in this thesis project. In addition, quantitative NO_2 laser-induced fluorescence, LIF, measurements in a plasma generated by electron beam in a sterilization rig at Tetra Pak are discussed and compared to electron dose simulations.

Hydrogen peroxide and water vapor are simultaneously visualized in a flow of vaporized H_2O_2/H_2O by using photofragmentation laser-induced fluorescence, PFLIF, and two-photon LIF, tp-LIF. It is found that OH fragments stemming from dissociation of H_2O is minor compared to OH fragments stemming from photodissociation of H_2O_2. A concept solely based on PFLIF is also discussed for simultaneous imaging of H_2O_2 and H_2O, which utilizes the spectral and temporal shape of the OH emission, stemming from photolysis of H_2O_2, to extract both water- and hydrogen peroxide mole fractions.

Structured illumination, SI, is combined with PFLIF to address issues that arise when the pump beam generates fragments of species that also are naturally present in the probe volume. The concept is demonstrated for imaging of hydrogen peroxides in a premixed laminar methane/air flame, where the pump beam is spatially intensity modulated and thereby giving the OH fragments a recognizable signature that allows them to be separated from naturally present OH radicals in the post processing of the image. The concept provides, for the first time, single-shot measurements of hydrogen peroxides in premixed laminar methane/air flames. Further, picosecond laser pulses both allow studies of OH production in the reaction- and product zone of the flame and at the same time minimizes the signal interference of chemically produced OH in the product zone, stemming from photochemistry of hot CO_2. The experimental results are compared with a chemical model, from where it is found that about 20 % of the oxygen fragments are formed in the singlet state, upon photolysis with picosecond laser pulses.

A detailed study of O_3 imaging using PFLIF is carried out in an ozone flow. The concept is also demonstrated on ozone produced by the gliding arc discharge. From experiments in the gliding arc discharge, it is found that the lifetime of hot O_2 is significantly shorter than the lifetime of O_3 and therefore the discharge was turned off, several microseconds prior to the arrival of the pump pulse. Nevertheless, the amount of naturally present hot O_2 produced by the discharge (for electrons with a kinetic energy of 0.8 eV) is estimated to be insignificant compared to the number of hot O_2, produced from photodissociation of O_3, and hence ozone imaging is also carried out when the discharge is operating.

Key words: Combustion diagnostics, Laser-induced fluorescence, Photofragmentation, Ozone (O_3), Hydroxyl radical (OH), Hydrogen peroxide (H_2O_2), Plasma

Classification system and/or index terms (if any)		
Supplementary bibliographical information		Language: English
ISSN and key title: 1102-8718		ISBN 978-91-7753-547-8 (print) ISBN 978-91-7753-548-5 (pdf)
Recipient's notes	Number of pages 157	Price
	Security classification	

I, the undersigned, being the copyright owner of the abstract of the above-mentioned dissertation, hereby grant to all reference sources permission to publish and disseminate the abstract of the above-mentioned dissertation.

Signature _____ Date 2018-01-16

Development of photofragmentation-based diagnostics

Kajsa Larsson

LUND UNIVERSITY

To whom it may concern

Content

Abstract

Development of photofragmentation-based diagnostic concepts for studying H_2O_2, H_2O, HO_2 and O_3 in three different measurement environments, i.e. a flow of vaporized H_2O_2/H_2O, a premixed laminar methane/air flame and a plasma, produced by a gliding arc discharge, are reported in this thesis project. In addition, quantitative NO_2 laser-induced fluorescence, LIF, measurements in a plasma generated by electron beam in a sterilization rig at Tetra Pak are discussed and compared to electron dose simulations.

Hydrogen peroxide and water vapor are simultaneously visualized in a flow of vaporized H_2O_2/H_2O by using photofragmentation laser-induced fluorescence, PFLIF, and two-photon LIF, tp-LIF. It is found that OH fragments stemming from dissociation of H_2O is minor compared to OH fragments stemming from photodissociation of H_2O_2. A concept solely based on PFLIF is also discussed for simultaneous imaging of H_2O_2 and H_2O, which utilizes the spectral and temporal shape of the OH emission, stemming from photolysis of H_2O_2, to extract both water- and hydrogen peroxide mole fractions.

Structured illumination, SI, is combined with PFLIF to address issues that arise when the pump beam generates fragments of species that also are naturally present in the probe volume. The concept is demonstrated for imaging of hydrogen peroxides in a premixed laminar methane/air flame, where the pump beam is spatially intensity modulated and thereby giving the OH fragments a recognizable signature that allows them to be separated from naturally present OH radicals in the post processing of the image. The concept provides, for the first time, single-shot measurements of hydrogen peroxides in premixed laminar methane/air flames. Further, picosecond laser pulses both allow studies of OH production in the reaction- and product zone of the flame and at the same time minimizes the signal interference of chemically produced OH in the product zone, stemming from photochemistry of hot CO_2. The experimental results are compared with a chemical model, from where it is found that about 20 % of the oxygen fragments are formed in the singlet state, upon photolysis with picosecond laser pulses.

A detailed study of O_3 imaging using PFLIF is carried out in an ozone flow. The concept is also demonstrated on ozone produced by the gliding arc discharge. From experiments in the gliding arc discharge, it is found that the lifetime of hot O_2 is significantly shorter than the lifetime of O_3 and therefore the discharge was turned off, several microseconds prior to the arrival of the pump pulse. Nevertheless, the amount

of naturally present hot O_2 produced by the discharge (for electrons with a kinetic energy of 0.8 eV) is estimated to be insignificant compared to the number of hot O_2, produced from photodissociation of O_3, and hence ozone imaging is also carried out when the discharge is operating.

Populärvetenskaplig sammanfattning

Lasern uppfanns på 1960-talet och har sedan dess fått många olika användnings-områden. Inom metallindustrin används laser främst för beskärning och svetsning, medan medicinska tillämpningar kan vara t.ex. ögonoperationer.

Laser och laserdiagnostik kan även användas för att förstå olika kemiska processer, däribland steriliseringsprocessen av en livsmedelsförpackning. En förståelse för hur steriliseringsprocessen går till kan spara både pengar och minska miljöpåverkan. Laserdiagnostik kan också användas inom förbrännings forskning där man på ett beröringsfritt sätt kan mäta förlopp, temperaturer och ämneskoncentrationer.

Syftet med att sterilisera en livsmedelsförpackning är att ta död på bakterier och mikroorganismer. Görs inte detta kan bakterier skada livsmedlet och produktens hållbarhet kan inte längre garanteras. Ur ett miljöperspektiv är det viktigt att minska onödig konsumtion av kemiska tillsatser samt fånga in och neutralisera skadliga ämen som uppkommer vid steriliseringsprocessen. Det är också viktigt att kunna garantera hållbarheten hos ett livsmedel för att undvika onödigt spill av mat och dryck som kan ha blivit förstörd av eventuella kvarvarande bakterier.

Att använda sig av modeller som beskriver verkligheten är ett relativt billigt sätt för att förstå olika processer. Istället för att krocka 100 bilar för att se vilken som klarar sig bäst i ett krocktest kan detta utföras i en dator genom modeller och simuleringar. För att kunna kontrollera att modellerna stämmer behöver dessa styrkas med experiment. Detta resulterar i att kanske 2 bilar måste krocktestas istället för 100 bilar, vilket sparar både tid och pengar.

Samma princip gäller för steriliseringsprocessen av livsmedelsförpackningar och inom olika förbränningsprocesser. Matematiska modeller och simuleringar kan göras för att förstå verkligheten, men de måste styrkas med experiment.
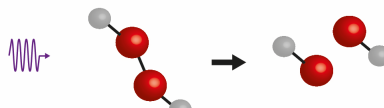
Ett laserkoncept kallat fotofragmentation laser-inducerad fluorescens (PFLIF) kan avbilda några av de ämnen som är relevanta för både förpackningsindustrin och inom förbränning och kan därmed användas för att styrka simuleringarna och modellerna. Två ämnen som i huvudsak har studerats i detta doktorandprojekt är väteperoxid, H_2O_2, och ozon, O_3. Metoden (för väteperoxid) går ut på att en laserpuls delar upp väteperoxidmolekylen i två OH radikaler. Därefter belyses OH radikalerna med ytterligare en laserpuls som tas upp av radikalen (absorberas) och en ljuspartikel, foton, sänds ut från radikalen som är specifik för just OH. De utsända fotonerna kallas fluorescens. Fluorescensen kan fångas in med hjälp av en kamera och man kan på så sätt se var OH radikalerna finns. Vet man var OH radikalerna är så vet man också

indirekt var väteperoxiden befann sig, eftersom man får två OH radikaler från varje väteperoxidmolekyl. Samma princip gäller för ozon där en laserpuls delar upp O_3 i en O atom och en O_2 molekyl medan en annan laserpuls belyser O_2 molekylen som sänder ut fluorescens, specifik för O_2.

Detta doktorandprojekt har i huvudsak handlat om att utveckla PFLIF metoden för att kunna avbilda H_2O_2 och O_3 i flammor och gaser. Exempelvis har OH radikalerna från H_2O_2 kodats för att kunna urskiljas från naturligt förekommande OH i flammor. Fluorescensen från OH har också studerats för att mäta vattenkoncentrationen i en gasblandning av H_2O_2 och H_2O.

PFLIF för H_2O_2 detektion

Fotodissociation
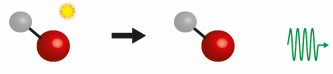
Då en laserpuls i UV (ultraviolett) området belyser H_2O_2 molekylen absorberas fotonen. Väteperoxidmolekylen kommer då att delas i två OH radikaler, eftersom bindningsenergin som håller ihop molekylen är mycket svag. Processen kallas fotodissociation.

Excitation

De två bildade OH radikalerna kommer inte skicka ut något ljus av sig själv utan måste belysas med en ny laserpuls. Varje molekyl och atom har ett eget "fingeravtryck" och kan endast absorbera fotoner av specifika våglängder. Det är därför viktigt att den insända fotonens våglängd kan absorberas av OH och därmed excitera radikalen. Bindningsenergin för OH är stark nog att kunna absorbera en foton i UV området utan att fotodissocieras.

Deexcitation och fluorescens

Den exciterade OH radikalen kommer sedan deexciteras, d.v.s. återgå till sitt ursprungliga tillstånd och sända ut en foton av en annan våglängd, så kallad fluorescens. Konceptet där en molekyl exciteras av en laserpuls och sänder ut fluorescens kallas laser-inducerad fluorescens (LIF).

List of papers

I. **K. Larsson**, O. Johansson, M. Aldén, and J. Bood, "*Simultaneous visualization of water and hydrogen peroxide vapor using two-photon LIF and photofragmentation LIF*", Applied Spectroscopy, 68(12), 1333-1341, 2014.

II. **K. Larsson**, M. Aldén and J. Bood, "*Simultaneous Visualization of Hydrogen Peroxide and Water Concentrations Using Photofragmentation Laser-Induced Fluorescence*", Applied Spectroscopy, 71(9), 2118–2127, 2017

III. M. Jonsson, **K. Larsson**, J. Borggren, M. Aldén and J. Bood, "*Investigation of photochemical effects in flame diagnostics with picosecond photofragmentation laser-induced fluorescence*", Combustion and Flame, 171, 59-68, 2016

IV. **K. Larsson**, M. Jonsson, J. Borggren, A. Ehn, E. Kristensson, M. Aldén and J. Bood, "*Single-shot photofragment imaging by structured illumination*", Optics letters, 40(21), 5019-5022, 2015

V. **K. Larsson**, D. Hot, A. Ehn, A. Lantz, W. Weng, M. Aldén and J. Bood, "*Quantitative Imaging of Ozone Vapor Using Photofragmentation Laser-Induced Fluorescence (LIF)*", Applied Spectroscopy, 71(7), 1578-1585, 2017

VI. **K. Larsson**, D. Hot, J. Gao, A. Ehn, C. Kong, M. Aldén and J. Bood, "*Instantaneous imaging of ozone in a gliding arc discharge using photofragmentation laser-induced fluorescence*", Submitted to Applied Physics D.

VII.   **K. Larsson**, H. Seyfried, U. Lindblad, M. Aldén and J. Bood, "*Quantitative NO₂ measurements in an industrial sterilization rig using laser-induced fluorescence*", Applied Industrial Optics: Spectroscopy, Imaging and Metrology, (Optical Society of America, Washington, DC, 2016), paper number: JW1F. 2.

Related work

VIII   E. Malmqvist, M. Jonsson, **K. Larsson**, M. Aldén, J. Bood, "*Two-dimensional OH-thermometry in reacting flows using photofragmentation laser-induced florescence thermometry*", Combustion and Flame, 169, 297-306, 2016

Abbreviations

Charge Couple Device	CCD
Computational Fluid Dynamics	CFD
DiMethyl Ether	DME
Equivalence ratio	φ
Fluorescence quantum yield	Φ
Fourier transform	F
Full Width at Half Maximum	FWHM
Homogeneous Charge Compression Ignition	HCCI
Infra-Red	IR
Intensified Charge Couple Device	ICCD
Krypton Fluoride	KrF
Laser-Induced Fluorescence	LIF
Laser Thomson Scattering	LTS
Optical Emission Spectroscopy	OES
PhotoFragmentation Laser-Induced Fluorescence	PFLIF
Plasma-Assisted Combustion	PAC
Rotational Energy Transfer	RET
Structured Illumination	SI
Two-dimensional	2D
Two-Photon Laser-Induced Fluorescence	tp-LIF
Ultra-Violet	UV
Universal Serial Bus	USB
Vibrational Energy Transfer	VET

Chapter 1

Introduction and motivation

The present work aims to develop laser-based techniques for *in situ* measurements, mainly of non-fluorescing molecules in various types of applications. Typically, three different measurement situations have been investigated in this thesis project, laminar gas flows, laminar premixed CH_4/air flames and plasmas. Except for NO_2 visualization in a plasma produced by electron bombardment or electron beam, all studies were conducted with a pump-probe technique called photofragmentation laser-induced fluorescence, PFLIF. Very briefly, in PFLIF the molecule of interest, say AB, is photodissociated into fragments A and B, whereupon fragment A is probed by laser-induced fluorescence, LIF. Hence, the PFLIF approach has a major challenge in terms of species specificity, which is schematically illustrated for species AB in Figure 1.1. Species A, B, C, AB and ABC are initially present in the probe volume. The pump-pulse wavelength is selected to photodissociate species AB into A and B fragments, but it may at the same time also photodissociate species ABC into A and BC fragments. After the arrival of the pump pulse, multiple species A, either formed by photodissociation of a parent species or naturally present, are found in the probe volume. At the arrival of the probe pulse, whose wavelength is chosen to match an absorption line of species A, any species A in the probe volume is excited and emitting fluorescence after relaxation. In order to be species specific PFLIF must be carried out in such a way that only A fragments stemming from photodissociation of AB are probed. A major focus of this thesis work has therefore been to improve the PFLIF technique so that it allows for species specific studies in environments relevant for combustion, plasmas and sterilization applications.

Up to now, two-dimensional (2D) imaging of hydrogen peroxides in combustion processes has been restricted to laminar premixed flames, since fluorescence from naturally present OH radicals interfere with signal of interest, i.e. fluorescence from OH fragments stemming from hydrogen peroxides, preventing single-shot imaging, a requirement for studies in turbulent environments [1]. It is, however, possible to overcome this limitation by spatially intensity modulating the pump beam, giving a recognizable signature to the created fragments, and then utilize a post processing

routine in the frequency domain, which extracts the desired fragment signal. This procedure has been described in Paper IV, where PFLIF has been combined with Structured Illumination, SI.
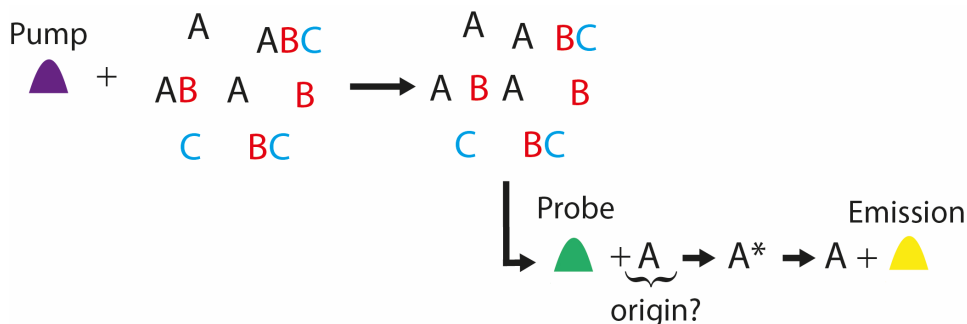
Figure 1.1. Schematic illustration of PFLIF of species AB in a probe volume containing species A, B, C, AB and ABC. The pump-pulse wavelength is selected to photodissociate AB into A and B fragments, while the probe-pulse wavelength is chosen to match an absorption line of species A, whose subsequent fluoresence is detected. However, naturally present species A together with A and BC fragments, also formed by photodissociation of ABC by the pump pulse, gives several A fragments that stems from various species in the probe volume. To determine the origin of the probed species A is therefore a major challenge in the PFLIF technique.

Furthermore, in hydrocarbon combustion photolysis of hot CO_2 also produces OH via oxygen fragments reacting with mainly H_2O and H. The intensity of the fluorescence from the chemically produced OH radicals is strongly dependent on the pump-probe delay time and a shorter delay time will suppress this chemical interference. This dynamic was investigated in the work presented in paper III, where PFLIF was carried out with picosecond laser pulses for delay times ranging between 0.5- and 22.5 ns.

   A similar study based on PFLIF has been carried out by Li *et al.* [2], in which CH_3 has been imaged in a CH_4/air flame. Here, CH_3 was dissociated using the 5th harmonic of an Nd:YAG laser at 212.8 nm, whereupon the created CH fragment was probed with a dye laser pulse at 426.8 nm. The authors found that the influence of naturally present CH in the flame was minor and they could therefore demonstrate single-shot measurements of CH_3. Hydrogen peroxide detection, using PFLIF, has been demonstrated in an HCCI engine [3]. Perhaps somewhat counterintuitive, the measurement task is, in a sense, easier in an engine than in a stationary flame, as the presence of hydrogen peroxides is separated in time from both OH radicals and CO_2, since hydrogen peroxides are precursors for the OH radicals and CO_2 is a final product. Therefore, interferences from naturally present OH and OH stemming from CO_2 photochemistry were of minor importance in the HCCI engine measurements reported in [3]. Osborn and Frank [4] reports detection of the vinyl, C_2H_3, radical and acetylene,

C₂H₂, in methane flames by using laser-induced fragmentation fluorescence with laser pulses of 230 nm wavelength. Laser-based techniques for studies of various intermediate species, relevant for combustion processes are described and discussed in the review articles by Aldén *et al.* [5], Kohse-Höinghaus [6] and Daily [7].
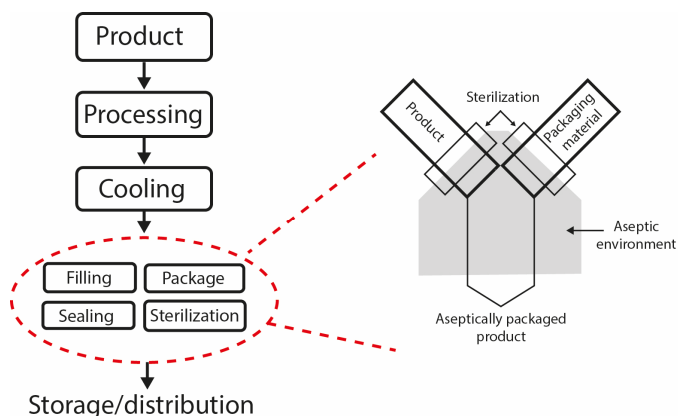
Figure 1.2. Flowchart of the major steps in aseptic food packaging adapted from [8,9], illustrating how a product is processed and cooled before enclosed in a sterilized container and ready for distribution. The left part of the figure shows how both the packaging material and the product are sterilized prior to integration in an aseptic envirnonment.

Shown in Figure 1.2 is a schematic illustration of the major steps in which a product is aseptically packaged. In this thesis work, one focus has been to improve the sterilization process, in which unwanted microorganisms are destroyed. In a paper by Laroussi [10] several sterilization approaches are described, such as sterilization by heat, gases, chemicals or radiation. Hydrogen peroxide, solved in water, is an example of an agent for chemical treatment used in many applications, for example in the food packaging industry. The reader is referred to Chapter 13 in the book by Robertson [8] for details regarding how H_2O_2 can be applied to aseptic food packaging. Further, in the food packaging industry, sensors based on absorption spectroscopy frequently determine species concentrations [11,12]. However, these sensors integrate along the line of sight and do not allow for 2D measurement which is a requirement for comparison with flow patterns and computational fluid dynamics, CFD, models. The chemistry between water and hydrogen peroxide is closely linked and simultaneous detection is of particular interest, and has previously been reported in the near infrared region [11,13,14]. In the work presented in Paper I, a concept for simultaneous imaging of H_2O_2 and H_2O based on PFLIF and two-photon LIF, tp-LIF, was developed and demonstrated. Furthermore, the ability to visualize two species simultaneously often requires two synchronized cameras and careful alignment of the laser beams. A concept based on PFLIF for quantitative imaging, where both the hydrogen peroxide and the

water vapor concentrations were extracted using only one camera, equipped with a stereoscope, was proposed. The concept, as presented in Paper II, is based on the fact that the OH fluorescence characteristics, spectrally and temporally, are dependent on the water concentration, while the total fluorescence intensity reflects the H_2O_2 concentration. However, the method requires that the two species are present in a bath gas that has low cross section for collisional quenching and vibrational energy transfer, VET, of electronically excited OH, for example argon. Although, the proposed technique may not be suitable for on-line assessment of food package sterilization, it might be feasible for research and development (R&D) facilities.

Furthermore, highly energetic electrons may also be employed as sterilization agent since they decontaminate surfaces having microbial contamination and thereby ensures food safety. In electron beam treatment, a plasma is created once the electrons interacts with ambient air and numerous reactive species such as ozone, O_3, and NO_2 are created. The electron beam technique is attractive for the food packaging industry since the generated plasma is non-thermal and thereby has an electron temperature that is much higher than the gas temperature. Due to the highly energetic electrons the deactivation of microorganisms is efficient, while the package is unaffected upon interaction with the cold gas temperature [15].

Stringent restrictions from health authorities require that reactive species like NO_2 need to be contained and neutralized. The need to understand how the reactive species are formed and thereby minimizing them is therefore urgent. In the study presented in Paper VII, quantitative LIF measurements have been employed to visualize NO_2 in a plasma created from an electron-beam rig at a research facility at Tetra Pak. In Figure 1.3 the experimental setup for NO_2 LIF measurements in the industrial test rig is shown. The mean concentration of NO_2 was found to agree well with gas analysis measurements performed at Tetra Pak.
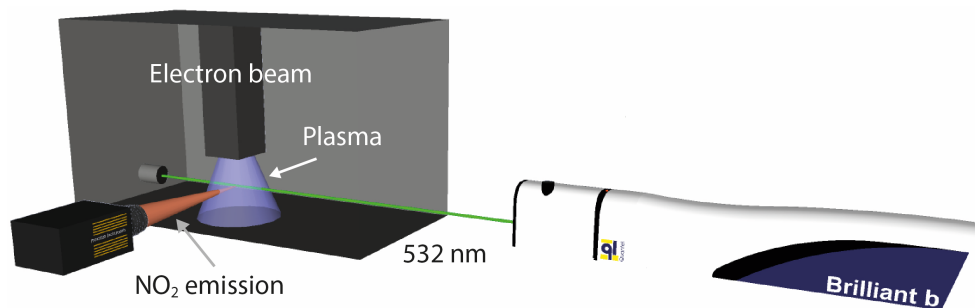
Figure 1.3. Illustration of NO_2 LIF measurements in an industrial electron-beam sterilization rig. The laser wavelength at 532 nm excites the NO_2 molecules in the plasma and the subsequent emission is detected by an ICCD camera positioned 90° relative to the laser beam propargation direction.

Imaging of O_3 is somewhat more complicated than NO_2 LIF as it requires a preceding photon that dissociates O_3 into vibrationally hot O_2 and O fragments, whereupon the hot O_2 fragment may be imaged using LIF. The PFLIF concept has been demonstrated for O_3 imaging in an ambient O_3 flow in the work presented in Paper V.

Recently, plasmas has gained significant interest in combustion research and plasma-assisted combustion, PAC, since they are capable of extending the explosion limit and stabilize flames under leaner conditions, which may reduce formation of pollutants and increase the combustion efficiency. Discussions regarding the prospects of PAC are found in the review article by Ju and Sun [16], where the authors discuss several plasmas and their properties and also provide an overview of the current research frontier of PAC. Optical diagnostic measurements is one way of extending the knowledge about plasmas, where Rayleigh scattering measurements for example may be used to study the gas temperature. By using an Nd:YAG laser Zhu *et al.* [17] have measured the gas temperature in a gliding arc discharge, which they found to be ~1100 K. For further information about optical diagnostics in non-thermal plasmas the reader is referred to the doctoral thesis by Jiajian Zhu [18] and the review article by Ryo Ono [19]. In the work presented in Paper VI, O_3 has been imaged in a plasma produced by a gliding arc discharge. In a similar manner as naturally present OH in flames interferes with OH fragments stemming from HO_2, plasmas produce hot O_2 that potentially may not be separated from hot O_2 fragments originating from photolysis of O_3. It was, however, found that the lifetimes of the two different O_2 contributions are vastly different, wherefore O_3 could be imaged interference-free with PFLIF in the gliding arc setup.

Chapter 2

Basic photophysics

Most species of interest in combustion research, e.g. OH, CH and NO have bound excited electronic states and may be detected using laser-induced fluorescence, LIF. Laser-induced fluorescence is a two-step process, where a photon whose energy corresponds to a transition of the molecule of interest is absorbed, followed by spontaneous emission, i.e. fluorescence [20]. There are species such as O_3, H_2O_2 and HO_2 that lack bound excited electronic states, accessible with UV/visible excitation, thus preventing them from direct detection using LIF. After electronic excitation follows fluorescence in the UV or visible region, which is where most imaging devices, such as CCD cameras, are sensitive. The following chapter reviews how photodissociation by a preceding UV laser pulse may be employed for imaging of O_3, H_2O_2 and HO_2.

2.1 Photofragmentation laser-induced fluorescence

Laser-induced fluorescence is a widely used technique for *in situ* detection of trace species, such as OH, NO and CH, and is used in various research fields, e.g. combustion diagnostics and atmospheric chemistry. These species have bound excited states, and therefore fluorescence can be emitted upon absorption of a photon in the UV or visible region. For species that lack bound electronic states, electronic excitation results in photodissociation into fragments. However, if a fragment is formed in an electronic excited state fluorescence can be collected upon relaxation to the ground state and the parent species can thereby be monitored indirectly. Nevertheless, fragments, having bound electronic states, and are formed in the ground state may be detected by a second photon using LIF.
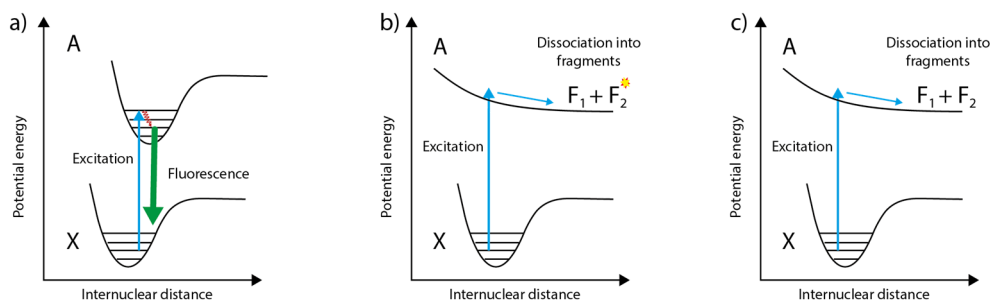
Figure 2.1.1. Scematic illustration of electronic excitation of a parent molecule, having a bound excited electronic state in a) and an un-bound excited electronic state in b) and c). In b) the excitation leads to dissociation into two fragments, F_1 and F_2, for which F_2 is formed in an excited state, whereas for c) the two fragments are formed in the ground state.

A schematic illustration of electronic excitation of a parent molecule is shown in Figure 2.1.1. In Figure 2.1.1a the excitation to a bound electronic state leads to fluorescence, whereas for Figure 2.1.1b and c the excitation leads to dissociation in which two fragments, F_1 and F_2, are formed. In Figure 2.1.1b fragment F_2 is formed in an excited state, while both fragments are created in the ground state in Figure 2.1.1c.

The concept, in which a pump photon photodissociates a parent molecule into fragments that are detected by a probe photon using LIF, is called photofragmentation laser-induced fluorescence, PFLIF. The PFLIF concept allows for indirect detection of non-fluorescing species and may also enable detection of larger molecules, often resulting in complex spectroscopy, by photodissociation into smaller fragments. In addition, the fluorescence signal from the fragments is proportional to the concentration of the parent molecule.

The PFLIF approach was first presented in the late 1970s and early 1980s by Rodgers *et al.* [21] and Davis *et al.* [22] for detection of atmospheric trace gases. There are three requirements for the PFLIF concept; the pump photon has to dissociate the parent molecule into fragments, at least one fragment need to have a bound electronic state and the probe photon has to match an absorption line of the fragment. Either one or two laser wavelengths may be used in the PFLIF concept. If one laser wavelength is used the laser pulse has to both photodissociate the molecule of interest and electronically excite one of the formed fragments. For the two-pulse PFLIF concept the pump- and probe processes may be separated, which allows for variation of the pump-probe delay time and can for instance be used in lifetime studies. However, for the one-pulse PFLIF approach, the pump-probe delay time is zero. Table 2.1.1 presents the three species, i.e. O_3, H_2O_2, and HO_2, which are treated in this thesis work, together with their respective photfragments as well as pump, probe and emission wavelengths.

Table 2.1.1. The three different species, treated in this thesis project, and the fragments formed upon photolysis with the specified pump pulse. The fragments are electronically excited with the probe pulse and subsequent fluoresence is monitored.

Species	Pump pulse (nm)	Fragments	Probe pulse (nm)	Emission (nm)
O_3	266/248 [23,24]	hot O_2^* + O	248 (hot O_2^*) [25]	250-400 [26]
H_2O_2	266/248 [23,24,27]	OH+OH	~283 (OH) [28]	305-320 [28]
HO_2	266 [23]	OH + O	~283 (OH) [28]	305-320 [28]

*Vibrationally excited

2.2 Photodissociation of O_3

The major photodissociation products formed by ozone photolysis below 1180 nm are listed in Table 2.2.1, of which $O(^1D)$ is formed at wavelengths below 411 nm and $O(^3P)$ is created at wavelengths longer than 411 nm [29].

Tabel 2.2.1. Products generated for different photon wavelengths after O_3 photolysis [29]. The wavelength regions represents the thermodynamic tresholds for fragmentation.

Wavelength (nm)	Products	Channel
$\lambda < 310$	$O(^1D) + O_2(a^1\Delta_g)$	1
	$O(^3P) + O_2(X^3\Sigma_g^-)$	2
$310 \leq\ < 411$	$O(^1D) + O_2(X^3\Sigma_g^-)$	3
$411 \leq\ < 463$	$O(^3P) + O_2(b^1\Sigma_g^+)$	4
$463 \leq\ < 612$	$O(^3P) + O_2(a^1\Delta_g)$	5
$612 \leq\ < 1180$	$O(^3P) + O_2(X^3\Sigma_g^-)$	6

In this thesis work, photon wavelengths of typically 248 nm have been used for photodissociation, thus producing the fragments $O(^1D)$ and $O_2(a^1\Delta_g)$. However, for wavelengths ranging from 240- to 300 nm the photodissociation yield for formation into channel 1 is 0.9, while the photodissociation yield is 0.1 for fragments to be formed in channel 2 [30]. Considering formation into channel 2, the O_2 fragments end up in high vibrational excited states, having varying population distributions depending on photodissociation wavelength. Geiser and coworkers [31] report population distributions between 226- and 266 nm, while Park and Slanger [30] discuss the

vibrational population distribution of 248 nm photolysis. Considering photodissociation wavelengths of 248- and 266 nm, the vibrational population distributions are similar and have a maximum between $v'' = 5$ and $v'' = 10$.

At laser wavelengths between 248.0- and 248.8 nm, corresponding to the tuning range of an injection-locked KrF excimer laser, the photon energies are high enough to electronically excite the $O_2(X^3\Sigma_g^-, v'' = 6, 7)$ fragments to the $O_2(B^3\Sigma_u^-, v' = 0, 2)$ states. For $O_2(B^3\Sigma_u^-, v' = 4)$ there is an overlapping repulsive state for which predissociation is the dominant loss factor [32]. Some fluorescence will, however, still be observable between 250- and 400 nm, where the emission is characterized by distinct peaks [25]. A schematic illustration of electronic excitation using 248 nm laser radiation, after photodissociation with the same laser pulse, is presented in Figure 2.2.1. The vibrational population distribution in the $O_2(X^3\Sigma_g^-)$ state is shown for photolysis with 248 nm laser light. The figure is adapted from [26] and the vibrational population distribution in the $X^3\Sigma_g^-$ state is adapted from [30].
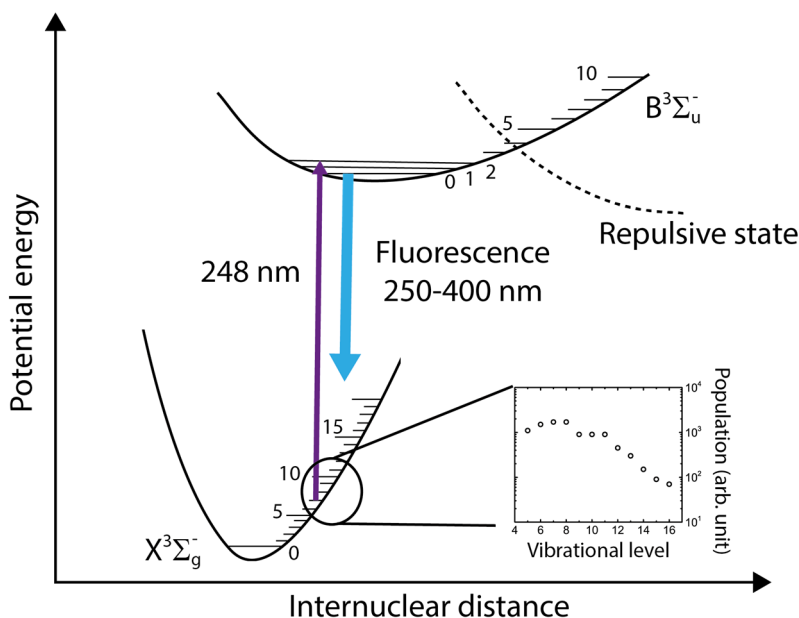
Figure 2.2.1. Schematic of electronic excitation of O_2 with 248 nm laser light, illustrated in an energy level diagram upon photodissociation of O_3 with the same laser pulse. The energy level diagram is adapted from [26] and the vibrational population distribution is adapted from [30].

The choice of both pump- and probe wavelengths are not restricted to 248 nm and could be selected in such a way that the created fragments can be probed using LIF. However, the absorption cross section of O_3 [29] as well as the population distribution in higher vibrational states of $O_2(X^3\Sigma_g^-)$ should be considered when selecting

dissociation wavelength. Furthermore, the PFLIF concept for ozone, where the vibrationally hot O_2 fragment is probed, is schematically illustrated in Figure 2.2.2. Predissociation of the electronically excited O_2 fragment is shown in the last step in Figure 2.2.2, where two oxygen atoms are formed.
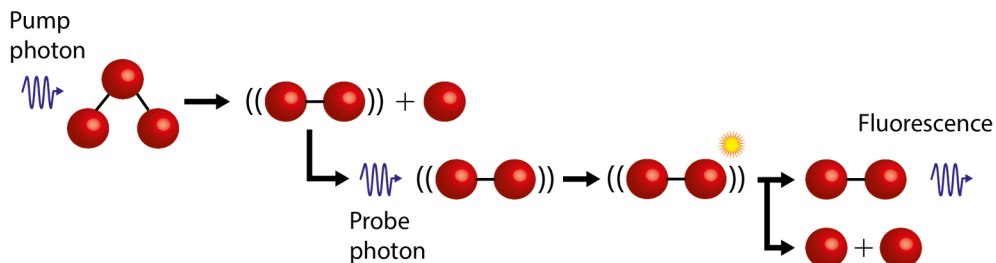
Figure 2.2.2. Schematic illustration of PFLIF of O_3. The pump photon photodissociates the ozone molecule into a vibrationally hot O_2 fragment and an oxygen atom, whereupon the probe photon electronically excites the vibrationally hot O_2 fragment, which after relaxation emits fluorescence between 250- and 400 nm. The dominant loss factor for the electronically excited O_2 fragment is predissociation and thereby two oxygen atoms are formed.

2.3 Photodissociation of H_2O_2 and HO_2

Hydrogen peroxide, H_2O_2 decomposes into fragments when absorbing a UV photon. The thermodynamic threshold for fragmentation is presented for wavelengths up to 557 nm in Table 2.3.1 [24]. In particular, the O-O bond is very weak and at wavelengths longer than 230 nm the quantum yield for OH production is two [23,33–35].

Table 2.3.1. Products generated for different photon wavelengths after H_2O_2 photolysis [24]. The wavelength regions represents the thermodynamic tresholds for fragmentation.

Wavelength (nm)	Products	Channel
< 197	$OH(A^2\Sigma) + OH(X^2\Pi)$	1
$197 \leq\ < 324$	$H_2O + O(^1D)$	2
$324 \leq\ < 359$	$HO_2 + H$	3
$359 \leq\ < 557$	$OH(X^2\Pi) + OH(X^2\Pi)$	4

The absorption cross section for H_2O_2 in the UV region is typically 10^{-20} cm^{-2} at 298 K and increases rapidly for decreasing photon wavelength [24]. In this thesis work typically 248- and 266 nm laser radiation have been used to photodissociate H_2O_2,

whereupon two OH($X^2\Pi$) fragments are formed in channel 4, since the quantum yield for OH production is two for these wavelengths. The OH fragments are probed using a second laser pulse, tuned to match an absorption line of the OH($A^2\Sigma^+$ ($v' = 1$) $\leftarrow$ $X^2\Pi$ ($v'' = 0$)) band at roughly 282-285 nm. A schematic illustration of PFLIF for H$_2$O$_2$ detection is depicted in Figure 2.3.1, where the pump photon is used for dissociation and the probe photon is used to electronically excite the formed OH fragment, whose subsequent fluorescence is monitored.
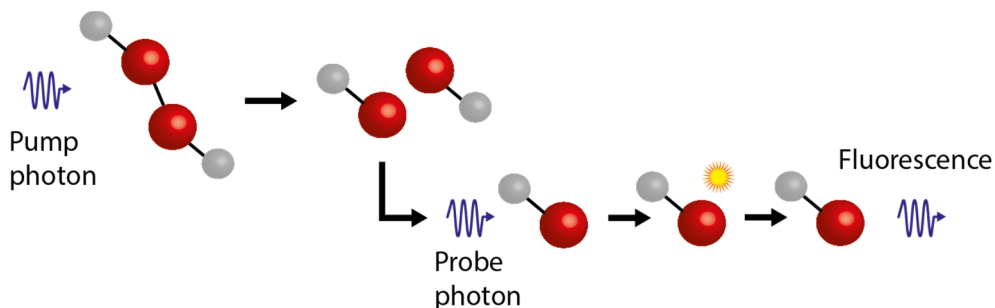

Figure 2.3.1. Schamatic illustration of PFLIF of H$_2$O$_2$. The pump photon dissociates the hydrogen peroxide molecule into two OH fragments, while the probe photon electronically excites one of the OH fragments. Fluoresence is emitted as the OH fragments relaxes to the ground state.

Furthermore, at short pump-probe delay times, typically tens of nanoseconds, the vibrational and rotational distributions of the nascent OH fragments need to be taken into account in order to tune the probe beam to match an absorption line of the fragments. For applications treated in this thesis work, the OH fragments are assumed to have a Boltzmann distribution at pump-probe delay times longer than 50 ns.

Some minor vibrational excitation into the $v'' = 1$ state of the nascent OH fragments has been reported for 193 nm photolysis, but has not been observed at 248- and 266 nm [33]. However, the rotational distribution of the OH fragments has been reported in [35,36], where it was found that the rotational distribution is cooler for 266 nm photolysis than for photolysis with 248 nm and 193 nm laser radiation.

There are five energetically allowed dissociation channels for HO$_2$ photolysis above 248 nm, where two forms OH + O(^{1}D)/O(^{3}P) and three generates H + O$_2$ in various configurations [37]. However, in the region 170-270 nm, corresponding to the $2^2A''$ $\leftarrow$ $1^2A''$ transition, the H + O$_2$ channel is very unlikely due to a potential barrier in the $2^2A''$ state [38]. A schematic illustration of PFLIF of HO$_2$ for the OH + O production channel is shown in Figure 2.3.2. For a photolysis wavelength of 220 nm, Sinah *et al.* [39], have found that the OH fragments end up in a rather cool rotational distribution of ~300 K, while only minor vibrational excitation was observed at this wavelength. Also, Hynes *et al.* [40] report similar observations upon 212 nm photolysis.
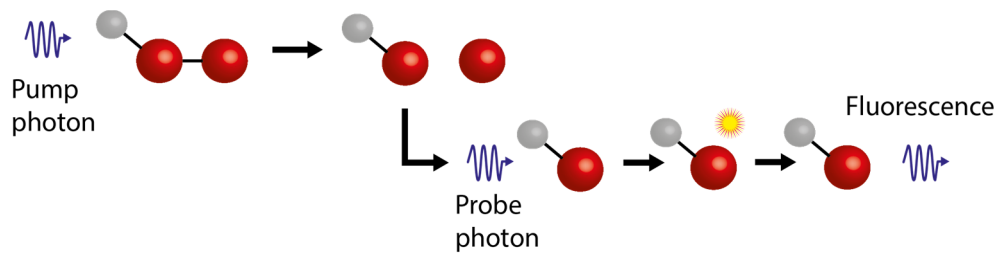
Figure 2.3.2. Schematic illustration of PFLIF of HO$_2$, where two fragments, OH and O, are formed upon photolysis. The OH fragment is probed using LIF.

Chapter 3

Simultaneous imaging of H_2O_2 and H_2O

In industrial applications such as the food packaging industry hydrogen peroxide is in a mixture with water. The present chapter will discuss two different laser based measurement techniques for simultaneous imaging of the two species. The two concepts are based on PFLIF of H_2O_2, where one combines PFLIF and two-photon LIF, tp-LIF, presented in Paper I, and the other utilizes the spectral shape of the OH fragment fluorescence to extract both the H_2O_2 and the H_2O concentration, see Paper II. Combining PFLIF and tp-LIF allows simultaneous imaging of the two species in ambient air, while the concept only based on PFLIF requires a bath gas whose collisional impact on the excited OH fragments is minimal. The tp-LIF approach will first be discussed briefly, followed by a detailed description of how the water vapor concentration is extracted from the spectral shape of the OH emission upon PFLIF of hydrogen peroxide. The chapter ends with a comparison of the two techniques.

3.1 The two-photon LIF approach

The PFLIF concept was combined with tp-LIF in order to perform simultaneous imaging of H_2O_2 and H_2O. A detailed description of the study is found in Paper I, and below follows only a brief presentation of the concept and the major conclusions. A KrF excimer laser, producing laser pulses at 248 nm was used to both dissociate H_2O_2 and excite the H_2O molecule. A schematic illustration of the technique is depicted in Figure 3.1.1. Figure 3.1.1a illustrates the processes at t = 0 when the 248 nm laser pulse is fired and Figure 3.1.1b illustrates the process at a certain time delay, typically 100 ns, when the probe pulse is fired. At t = 0 the H_2O_2 molecule is dissociated into two OH fragments by one 248 nm photon. Also, at t = 0 two photons at 248 nm, corresponding to the energy of one photon at 124 nm, simultaneously excites the H_2O

molecule into a predissociative state, which upon relaxation emits broadband fluorescence between 400- and 500 nm. Since excitation occurs to a predissociative state the H_2O molecule can dissociate into O and OH* (the asterisk indicates that the particle is electronically excited) and fluorescence is emitted between 305- and 320 nm as the OH fragment relaxes to its ground state. Within a couple of nanoseconds three OH fragments, one stemming from H_2O and two originating from H_2O_2, will thus be present in the measurement volume. At the arrival of the probe pulse, typically 100 ns after the 248 nm pulse, the OH fragments may not be separated from each other, see Figure 3.1.1b.

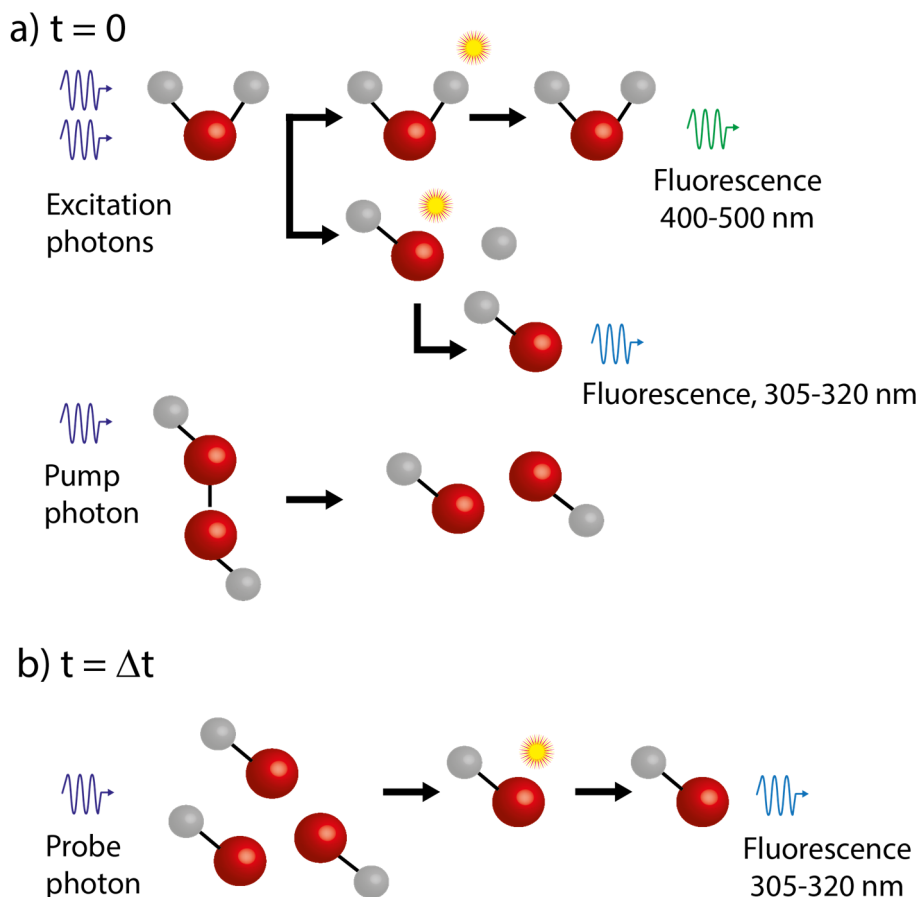**Figure 3.1.1.** The 248 nm laser pulse is fired at t = 0 presented in a), where two photons simultaneously excite the H_2O molecule into a predissociative state where the molecule may dissociate into O and OH. The H_2O_2 molecule is also dissociated into two OH radicals at t = 0. At a certain time delay after the pump pulse is fired, illustrated in b), the probe pulse excites all the OH radicals in the probe volume.

In order to assess the diagnostic potential of the measurement concept, an important part of the work, presented in Paper I, was to investigate the magnitude of the signal from OH fragments, stemming from H_2O, compared to the OH signal originating from H_2O_2. It was found that the OH signal from H_2O was negligible, thus allowing simultaneous imaging of the two species. The study was performed in a vaporized H_2O_2/H_2O/air mixture at room temperature and there is a linear dependence between signal intensity and mole fraction for H_2O and H_2O_2, respectively.

3.2 OH emission for extraction of H_2O concentration

In Paper II a measurement concept for simultaneous imaging of H_2O_2 and H_2O is presented, where the characteristics of OH emission stemming from H_2O_2 is utilized to extract both the H_2O_2 and the H_2O concentrations. Imaging of H_2O_2 is employed by capturing the total OH fluorescence in the same manner as presented in Paper I. For a thorough description of PFLIF of H_2O_2 the reader is referred to Paper II or the photophysics section 2.3 in this thesis. The study was performed using nanosecond laser pulses in a vaporized mixture of H_2O_2/H_2O, having argon as bath gas. Extracting the water mole fraction from the OH emission requires that the mixture is in a bath gas with minimal collision cross section of OH*, thus argon was employed. Two measurement scenarios are presented in Figure 3.2.1a where the spectral shape of the OH emission, having the probe laser wavelength tuned to the A^2X^+ $(v'=1) \leftarrow X^2\Pi$ $(v''=0)$ band of OH, is shown for argon and nitrogen bath gases in the upper and lower panels, respectively. For nitrogen bath gas the emission is dominating in the 0-0 band, whereas for argon fluorescence is emitted in both bands. To explain the spectral appearance in Figure 3.2.1a, an energy level diagram of OH with the transitions of interest indicated, is presented in Figure 3.2.1b. Here, the blue and red arrows indicate the spontaneous emission, i.e. fluorescence, in the 0-0 and 1-1 band, with spontaneous emission Einstein coefficients A_{00} and A_{11}, respectively. The probe laser, operating at roughly 282 nm, excites the OH fragments from its ground state, $v''= 0$, to the excited state, $v' =1$, indicated by the black arrow, *Exc.*, in Figure 3.2.1b. The quenching rates are denoted Q_{00} and Q_{11}, while the vibrational energy transfer is denoted, *VET*. In a bath gas such as nitrogen the *VET* process is fast, due to its relatively high collisional *VET* cross section, and just about all emission therefore ends up in the 0-0 band. For a bath gas such as argon, for which the *VET* cross section is very low emission arises only in the 1-1 band. The reason why we get emission in both bands when argon is employed is essentially due to that the *VET* process is fast for water and hence will put significant population in the 0-0 band.

Only a fraction of the excited molecules contributes to the detected fluorescence signal since molecular collisions give rise to energy losses. These energy losses occurs under molecular collisions when electrical energy is transferred to the surrounding,

preventing fluorescence from the excited state, hence the term *quenching*. The molecular interaction with the environment determines the quenching rate and hence, collisional quenching strongly depends on colliding partners, temperature and pressure of the mixture and is described by

$$Q = \sum_i q_i N_i. \qquad (3.2.1)$$

Here, q_i is the quenching rate constant for species i and N_i is the number density of species i. In a similar manner, the *VET* process also depends on interaction upon molecular collisions and is given as

$$VET = \sum_i k_i N_i, \qquad (3.2.2)$$

where k_i is the vibrational energy transfer rate constant for species i. Consequently, the excited molecule transfers energy to the environment as it de-excites to a lower vibrational state, thus dispersing the fluorescence spectrum. The fine structure in the fluorescence spectrum is increased even further by rotational energy transfer, *RET*, which is a result of molecular collisions in which energy losses to the surrounding put significant population in lower rotational states. The *RET* process will not contribute significantly to the total fluorescence intensity in the vibrational bands in the presented study and will therefore not be discussed further.

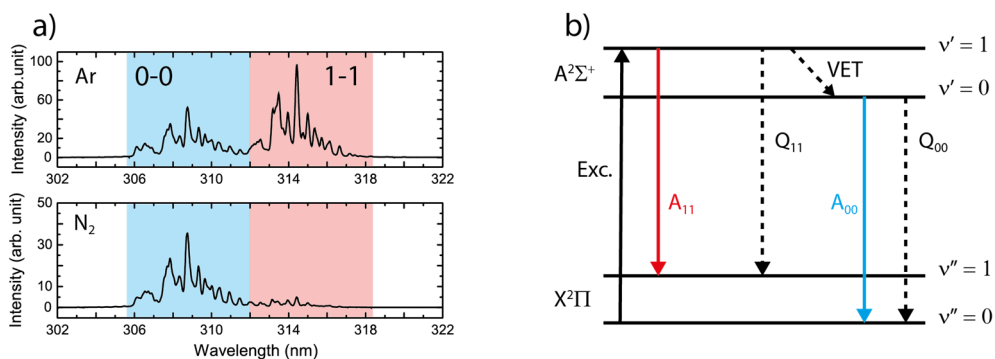**Figure 3.2.1.** Emission distribution in the 0-0 and 1-1 band of OH respectively is shown in a). When argon, having low cross section for collisional quenching, is employed as bath gas there is significant population in both emission bands as seen in the upper panel of a), whereas the emission is dominating in the 0-0 band for nitrogen bath gas. Energy level diagram for the transitions of interest of OH is presented in b).

Furthermore, the water vapor concentration in the mixture was roughly 1.5 %, high enough to allow the water molecules to contribute to *VET* and quench the OH fluorescence signal. On the contrary, the H_2O_2 concentration was less than 500 ppm and did not quench the fluorescence or affect the *VET* process significantly. Potential quenching and *VET* due to collisions with H_2O_2 have therefore been neglected.

The main idea of the work presented in Paper II is to investigate how the OH emission spectrum depends on the water vapor concentration and its potential as a diagnostic tool. Since water vapor is the main colliding partner in the mixture the number density of water molecules will affect Q_{11}, Q_{00}, and *VET*, see Figure 3.2.1b. To start with, expressions of fluorescence quantum yields have to be derived for the emission bands. The fluorescence quantum yield for a specific emission band is defined

$$\Phi = \frac{\#\ of\ fluorescence\ photons\ emitted\ in\ the\ specific\ band}{\#\ of\ absorbed\ photons} \tag{3.2.3}$$

and is hence a fraction $0 \leq \Phi \leq 1$. An alternative, yet equivalent, formulation of the fluorescence quantum yield is

$$\Phi = \frac{fluorescence\ rate\ in\ the\ specific\ band}{sum\ of\ the\ rates\ for\ all\ possible\ deactivation\ channels}. \tag{3.2.4}$$

In the four-level diagram, see Figure 3.2.1b, the fluorescence quantum yield for emission to end up in the 1-1 band is given by

$$\Phi_{11} = \frac{A_{11}}{A_{11} + Q_{11} + VET}. \tag{3.2.5}$$

The expression for Φ_{00} will be somewhat more complicated since the quantum yield for population to end up in $v' = 0$ has to be considered. Nevertheless,

$$\Phi_{00} = \Phi_{v'=0} \cdot \frac{A_{00}}{A_{00} + Q_{00}} \tag{3.2.6}$$

with

$$\Phi_{v'=0} = \frac{VET}{A_{11} + Q_{11} + VET} \tag{3.2.7}$$

giving a final expression for Φ_{00}

$$\Phi_{00} = \frac{VET}{A_{11} + Q_{11} + VET} \cdot \frac{A_{00}}{A_{00} + Q_{00}}. \tag{3.2.8}$$

An expression for the ratio between the two fluorescence quantum yields may now be expressed as

$$\frac{\Phi_{11}}{\Phi_{00}} = \frac{A_{00} + Q_{00}}{VET} \cdot \frac{A_{11}}{A_{00}}. \tag{3.2.9}$$

The A_{00} and A_{11} coefficients are well known constants of $1.45 \cdot 10^6$ s^{-1} [28] and $8.68 \cdot 10^6$ s^{-1} [28] respectively, while expressions for Q_{00} and VET will be discussed. For the present mixture the colliding partners are argon and water vapor giving a total quenching rate

$$Q = q_{QAr}[Ar] + q_{QH2O}[H_2O], \tag{3.2.10}$$

Where [Ar] and [H₂O] are concentrations of argon and water, respectively. It is important to consider the temperature and the rotational distribution of the OH fragments when selecting q. In the study presented in Paper II, the VET process puts significant population in high rotational states of $v' = 0$ and q was therefore chosen accordingly, whereas for $v' = 1$ thermal values were selected.

The total VET rate in the mixture is given by

$$VET = k_{Ar}[Ar] + k_{H2O}[H_2O]. \tag{3.2.11}$$

It should be pointed out that the VET rate constants also should be selected according to the temperature of the mixture and the rotational distribution in $v' = 0$. The quenching- and VET rate constants for argon and water, respectively, can be found in the literature and are also described in Paper II for the two excited states. Further, the total number density in the mixture, according to the ideal gas law, is calculated as

$$N_{tot} = \sum_i N_i = 2.49 \cdot 10^{19} \; cm^{-3} \tag{3.2.12}$$

at ambient conditions. By letting a variable, x, denote the water vapor concentration in the mixture, the concentration of argon will be $(1-x) \cdot N_{tot}$ (The very low concentration of H₂O₂ is neglected). Using this variable and Equation 3.2.10, 3.2.11 and 3.2.12 expressions for Q_{00}, Q_{11}, and VET can be written as

$$Q_{00}(x) = N_{tot}[q_{Ar}^0(1-x) + q_{H2O}^0 \cdot x], \tag{3.2.13}$$

$$Q_{11}(x) = N_{tot}[q_{Ar}^1(1-x) + q_{H2O}^1 \cdot x], \tag{3.2.14}$$

$$VET(x) = N_{tot}[k_{Ar}(1-x) + k_{H2O} \cdot x], \tag{3.2.15}$$

where q_{Ar}^0, q_{H2O}^0, q_{Ar}^1 and q_{H2O}^1 denotes the quenching rate constants for the $\nu' = 0$ and $\nu' = 1$ states respectively. Finally, considering Equation 3.2.13 and 3.2.15, and that $Q_{00} \gg A_{00}$, Equation 3.2.9 can be rewritten as

$$\frac{\Phi_{11}}{\Phi_{00}} = \frac{A_{11}}{A_{00}} \cdot \frac{q_{Ar}^0(1-x) + q_{H2O}^0 \cdot x}{k_{Ar}(1-x) + k_{H2O} \cdot x}. \tag{3.2.16}$$

Note, that the ratio between the fluorescence quantum yields of the two bands is only dependent on the water vapor concentration, x, in the mixture.

The model, presented in Equation 3.2.16, was validated by measuring the relative fluorescence intensity in the 0-0 and 1-1 band, see Figure 3.2.2. Here, the circular dots are experimental data points obtained in mixtures containing H_2O_2/H_2O ranging from 29-435 ppm H_2O_2 and 1.43-2.45 % H_2O, respectively. The black solid line represents a calculation using Equation 3.2.16, i.e. corresponding to argon as bath gas, while the dashed lines represents calculations assuming nitrogen or air as bath gas. It is clearly seen in Figure 3.2.2 that the sensitivity is much higher for the technique when argon is employed as bath gas, which essentially is due to that the *VET* process is about 50 times higher for nitrogen bath gas.
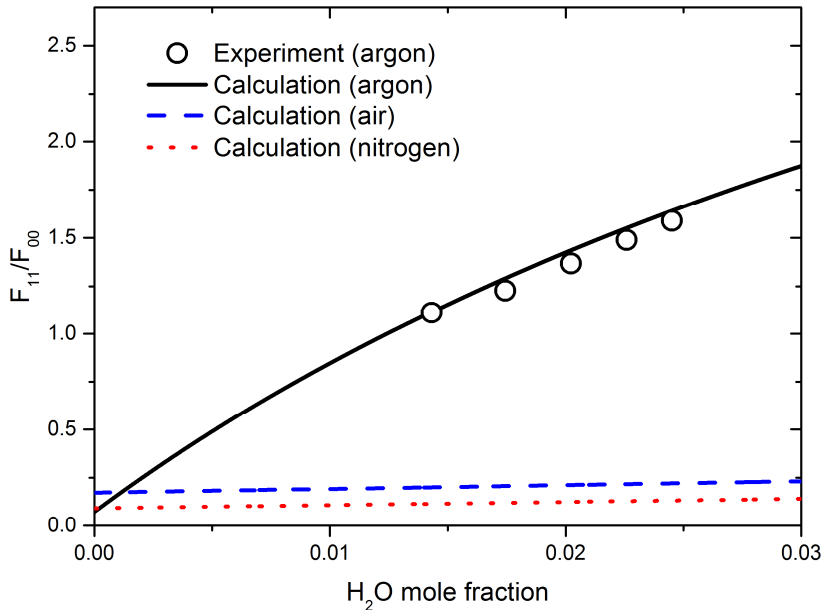

Figure 3.2.2. Experimental data points of the relative fluorescence intensity in the 1-1 and 0-0 band. The black solid line represents the model presented in Equation 3.2.16, whereas the dashed lines are calculations when air or nitrogen are employed as bath gases.

Furthermore, the good agreement between the experimental data points and the model clearly suggests that the water vapor concentration can be extracted from the spectral shape of the OH fluorescence stemming from H_2O_2. In Figure 3.2.3, the ratio between the fluorescence bands as a function of water mole fraction, based on Equation 3.2.16, is depicted for several species, such as nitrogen, argon and helium. In the simulation the corresponding quenching constants have been used for helium; $q_{He}^0 = 2 \cdot 10^{-11}$ cm^3/s [41] and $k_{He} = 5 \cdot 10^{-14}$ cm^3/s [41]. In Figure 3.2.3a the full region is shown for helium, argon, nitrogen, air and a mixture of N_2:Ar (20:80). Here, it can be seen that the sensitivity, i.e. the gradient, for argon and helium is largest for small water mole fractions, while air and nitrogen have higher sensitivity when the water mole fraction is increased. For diagnostic applications the sensitivity should be as high as possible for the region of interest and bath gas mixtures may then be employed that fulfill these demands.
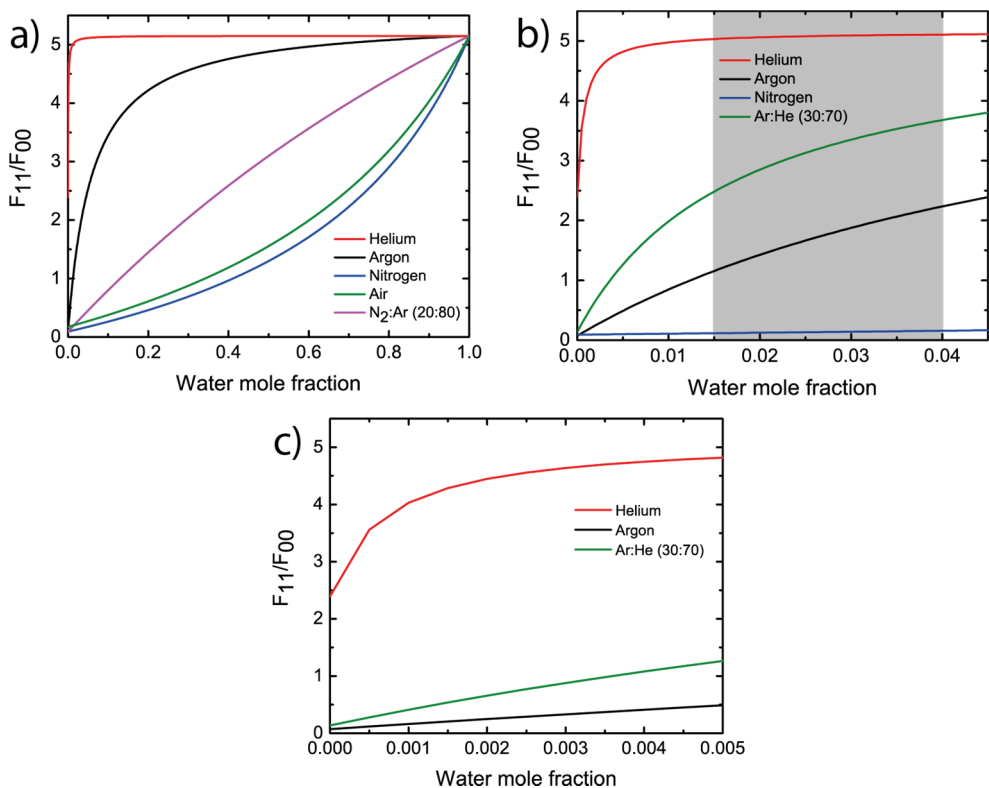

Figure 3.2.3. Simulations of the ratio between the fluorescence bands as a function of water mole fraction and various species. Here, a), b) and c) shows water mole fractions ranging 0-1, 0-0.045 and 0-0.0005, respectively. The gray area in b) represents water mole fractions typically used in the food packaging industry.

In Figure 3.2.3a an example of a gas mixture of N_2:Ar (20:80) is shown, where the sensitivity is similar for the whole range. In the food packaging industry typically water mole fractions ranging between 0.015 and 0.04, indicated by the gray area in Figure 3.2.3b, is used. For this interval the sensitivity is rather good for argon bath gas, but may be increased even further if argon is mixed with helium, as indicated by the green curve for a mixture of Ar:He at (30:70). If pure helium bath gas is employed the sensitivity is very good for low water mole fractions as presented in Figure 3.2.3c. The technique may thus be feasible for mixtures having low water concentration.

The proposed concept requires that the 0-0 band is separated from the 1-1 band, which may be achieved by using a spectrograph or a sharp band-pass filter in front of the detector. The experimental data points shown in Figure 3.2.2 have been extracted by integrating the intensity in both bands. A spectrograph integrates the measurement volume without any information about spatial resolution, yielding unambiguous interpretation of the data. The ability to visualize flow patterns is important when comparing with CFD models, thus 2D measurements using a camera is required. Utilizing a spectral filter, having a sharp transmission edge at 312 nm, allows imaging of the two bands. Such a setup, either using two cameras or one with a stereoscope allows 2D visualization. The temporal behavior of the OH emission may also be utilized to separate the two bands and will be discussed in the next section.

3.2.1 Temporal behavior of the OH emission

As already alluded to in the previous section the emission bands need to be separated in order to extract the water vapor concentration. The emission intensity reflects the population distribution in each band. At t = 0, v' = 1 has a population of n, i.e. $N_1(0)$ = n, whereas v' = 0 has no population, i.e. $N_0(0)$ = 0. Considering the energy level diagram in Figure 3.2.1b the time dependent decrease in v' = 1 is given by

$$\frac{dN_1}{dt} = -(Q_{11} + A_{11} + VET) \cdot N_1,$$
(3.2.17)

while the change in v' = 0 is described as

$$\frac{dN_0}{dt} = VET \cdot N_1 - (Q_{00} + A_{00}) \cdot N_0.$$
(3.2.18)

The fluorescence intensity in each band is given by the population times the Einstein coefficient. By solving the differential equations, Equation 3.2.17 and 3.2.18, the following expressions give the relation between water vapor concentration and the fluorescence intensities as a function of time

$$F_{11}(t,x) = n \cdot A_{11} e^{-\left(Q_{11(x)} + A_{11} + VET(x)\right)t},$$
(3.2.19a)

$$F_{00}(t,x) = n \cdot A_{00}\left[e^{-(Q_{00}(x)+A_{00})t} + e^{-(Q_{11}(x)+A_{11}+VET(x))t}\right]. \qquad (3.2.19b)$$

In Figure 3.2.4a the total fluorescence intensity is presented for argon bath gas using Equation 3.2.19a and b. Here, the curves represents five different water mole fractions, indicated by the legend. The total fluorescence intensities in Figure 3.2.4a have been convoluted by a 8 ns (FWHM) Gaussian curve that represents the probe laser pulse. The lifetime, τ, of the fluorescence was calculated from the slope of the different water mole factions as $A = A_0 \cdot e^{-t/\tau}$, where $\tau = -t/\ln(A/A_0)$. The result is shown in Figure 3.2.4b as the black squares, whereas experimental data points are shown as red circles. Although, the uncertainty of the experimental points is rather big, the trend is clear for both the simulation- and experimental data points, i.e. higher water concentration gives a shorter fluorescence lifetime, which is expected since the quenching is larger when the water concentration is increased.
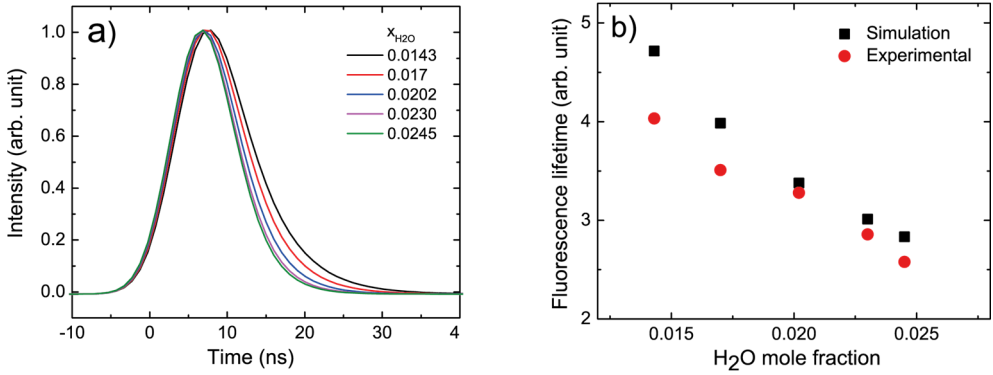
Figure 3.2.4. Normalized total fluorescence intensities is shown in a), calculated using Equation 3.2.19 a and b for five different water concentrations. Lifetimes of the OH signals is presented in b), where the black squares are from the simulation in a) and the red circles are experimental data points.

3.3 Comparison of the two techniques

In this chapter, two laser based measurement techniques aiming to perform simultaneous imaging of H_2O_2 and H_2O have been discussed. In Table 3.3.1. the major differences between the concepts are summarized. A drawback, with the PFLIF concept is the requirement of a mixture having a bath gas that has minimal collisional impact, i.e. both *VET* and quenching on the excited OH fragments. In applications such as sterilization of food packages, typically air is employed as bath gas. The use of laser diagnostics is, however, not necessarily intended as an on-sight measurement technique, but rather as a tool for research and development of sterilization rigs. Test rigs at research facilities may thus operate on bath gases such as argon, allowing

simultaneous imaging of H_2O_2 and H_2O based on the PFLIF concept. If a spectral filter having a sharp transmission edge at 312 nm is employed both H_2O_2 and H_2O concentrations may be extracted using one camera with a stereoscope. Also, the wavelength of the pump laser is not restricted to a resonant transition, which is the case for water vapor, since the absorption spectra of H_2O_2 is broad and virtually featureless [23], and could be selected according to availability and budget. In test rigs at research facilities, compact and non-complex experimental setups are feasible. Further, narrowband lasers having high peak power that produces pulses of roughly 248 nm are often large, ponderous and expensive, thus limiting the tp-LIF technique for practical applications. The reduction of experimental equipment, cost, and pixel-to-pixel overlap between cameras strongly motivates the PFLIF approach for practical applications. Nevertheless, one should bear in mind that apart from the requirement of argon bath gas the OH LIF process has to be linear, which requires that the OH fragment concentration is sufficiently high since the probe laser intensity has to be kept relatively low, thus the technique is restricted to mixtures having rather high H_2O_2 concentration.

Table 3.3.1. Comparing the major differences between the presented concepts in Paper I and Paper II.

	PFLIF combined with tp-LIF	PFLIF
Bath gas	Not critical	Restricted to bath gases that has low cross section for collisional quenching, like argon.
Detection equipment	Two cameras	Two cameras or one with a stereoscope.
Pump laser wavelength	Absorption peak of H_2O, roughly at 248 nm	Any wavelenght that dissociates the H_2O_2 molecule [23].
OH fluorescence in the linear regime	Not required	Yes
Detection limits for single-shot imaging	H_2O: 0.1 % H_2O_2: 5 ppm	H_2O: 0.05 % H_2O_2: 20 ppm

The detection limits for the techniques are presented in Table 3.3.1 and should be considered for applications in which the H_2O_2 concentration is low. The combined tp-LIF and PFLIF concept is then preferable, since the OH LIF process does not have to be in the linear regime. Although, the PFLIF concept having helium as bath gas may be preferable if the H_2O_2 and H_2O concentrations are low since the detection limits are increased further with low collisional quenching from helium on the OH fluorescence. In most practical applications such as the food packaging industry, the H_2O_2 and H_2O concentrations are typically one or two orders of magnitude larger than the detection limits presented here and hence, detection limits do not have to be considered. However, for these applications the hydrogen peroxide concentration is typically 0.5-2 % and thus may not be neglected as a quencher of the OH fluorescence. For applications in which the hydrogen peroxide concentrations is high enough to

significantly quench the OH fluorescence the tp-LIF and PFLIF concept should be employed.

In conclusion, aspects such as H_2O_2 and H_2O concentrations, experimental setup and bath gas, have to be considered when planning simultaneous imaging experiments of H_2O_2 and H_2O and thus, appropriate measurement technique may be selected.

Chapter 4

Flame studies

In the present chapter, two studies based on PFLIF, for measuring mainly HO_2 in premixed flames are presented. The main challenge of imaging HO_2 in premixed hydrocarbon flames is the large amount of naturally present OH in the flame, which will interfere with the created OH fragment signal upon dissociation of HO_2. In addition, interfering OH signal will also stem from chemical reactions that are induced by the pump pulse. In the first presented study, see Paper IV, PFLIF have been combined with structured illumination, SI, in order to eliminate the signal from naturally present OH, allowing single-shot measurements. In the second study, see Paper III, picosecond laser pulses are employed to temporally investigate the OH production, induced by the pump pulse, in the flame. Prior to presenting the laser-based techniques, previous works on HO_2 imaging in flames are introduced.

4.1 PFLIF in a CH_4/air flame

Traditionally, laser-based techniques have been used to visualize species in flames [5–7]. For H_2O_2 and HO_2 imaging, PFLIF may be employed. The interested reader will find details regarding PFLIF of hydrogen peroxides in the photophysics section 2.3. Hydroxyl radicals are, however, also naturally present in hydrocarbon flames, leading to fluorescence that interferes with the fluorescence from OH fragments produced by PFLIF of mainly HO_2 [1], thus posing a big challenge in separating the fluorescence signals. Johansson *et al.* [1] first proposed and demonstrated PFLIF of HO_2 in flames using nanosecond laser pulses. In their work a PFLIF image was taken, see Figure 4.1.1a, with both pump- and probe pulses fired. The PFLIF image contains OH signal stemming from both hydrogen peroxides and naturally present OH in the flame. In addition, a second image, LIF, was acquired with only the probe laser fired, as presented in 4.1.1b, thus containing only fluorescence from naturally present OH. Subtraction of the two images (PFLIF-LIF) gives the OH fragment signal presented in Figure

4.1.1c. It is clearly seen that Figures 4.1.1a and 4.1.1b looks virtually the same and the difference of the images is therefore delicate and must be used and interpreted with great care. The two images are acquired subsequently, thus the technique is highly sensitive to both laser pulse fluctuations and flame variations, and the method is therefore restricted to stable laminar flames, where signal averaging may be applied. The fact that two images have to be recorded prevents single-shot measurements, which is a requirement for studies in non-stationary environments. A method based on structured illumination was therefore developed, aiming at instantaneous measurements of hydrogen peroxides in flames, and this work is presented in Paper IV.

Further, the final image, shown in Figure 4.1.1c, suffers from signal in the product zone, which according to Johansson *et al.* [1] was found to be fluorescence stemming from OH produced by chemical reactions upon photolysis of hot CO_2. The intensity of this photochemically induced OH signal is strongly dependent on the pump-probe delay time. Johansson *et al.* [1] investigated the signal for pump-probe delays times between 10 ns and 100 μs, whereas in Paper III the use of picosecond laser pulses enabled studies at delay times shorter than 10 ns. The chemical interference at short pump-probe time delays is investigated in Paper III and will be further discussed in section 4.3.
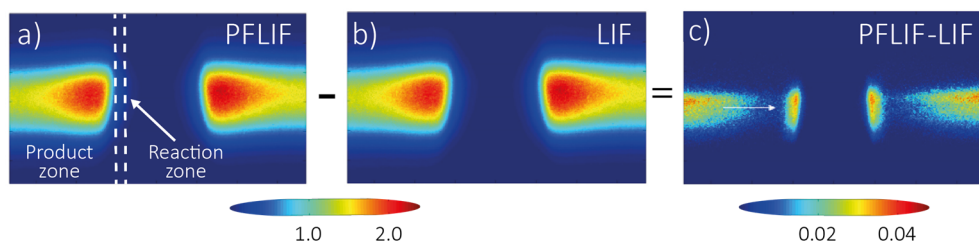

Figure 4.1.1. PFLIF of hydrogen peroxides in flames adapted from [1]. In a) both pump- and probe pulses are fired, in b) only the probe pulse is fired and in c), the LIF image have been subtracted from the PFLIF image. The OH fragments stemming from hydrogen peroxides are clearly seen in the reaction zone in c), whereas OH stemming from chemical interference is located in the product zone. Note, the intensity scale for a) and b) is roughly 50 times higher than the intensity scale in c).

4.2 Structured illumination

A concept based on combining PFLIF and structured illumination, SI-PFLIF, was developed and used for imaging of hydrogen peroxides in flames. Structured Illumination was first proposed to remove out-of-focus intensity contributions in microscopy imaging [42]. Three different intensity modulated images were projected onto the in-focus plane, and a final image could be extracted by combining the three

images in such a way that the out-of-focus light was minimized. This three-image-configuration prevents single shot imaging, a requirement for imaging in turbulent environments, and was therefore combined with a spatial-frequency lock-in method to overcome this limitation [43]. In this thesis work further improvement of the spatial frequency lock in algorithm presented in [43] was established. For an extended review of SI the reader is referred to the Doctoral thesis of Elias Kristensson [44]. The present study was conducted in such a way that the OH fluorescence, stemming from CO_2 photolysis, in the product zone was excluded in the images. This was established by crossing the laser beams, and is schematically illustrated in Figure 4.2.1. Here, the pump laser beam is turned into a sheet by a cylindrical lens before it propagates through a metallic transmission grating, with a line separation of 0.3 mm, which encodes the laser beam. The probe-laser beam is also converted into a sheet by a cylindrical lens and overlapped with the pump-laser beam in the reaction- and unburned zones of the flame.
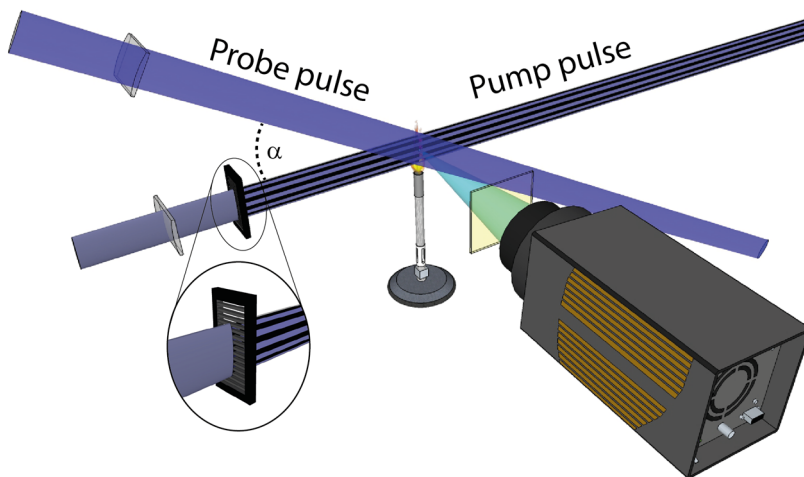

Figure 4.2.1. Schematic illustration of the experimental setup presented in Paper IV.

A PFLIF image was first recorded, I_{RAW}, where the intensity modulated pump beam and the probe beam were fired, see Figure 4.2.2a. A circular filter was then multiplied with the acquired I_{RAW} to prevent sharp edges, having multiple frequencies in the frequency domain, from interfering with the signal of interest. Intensity modulating the pump beam gives the OH fragments a recognizable signature that can easily be identified in the frequency domain. By turning I_{RAW} to the frequency plane by Fourier transformation, see Figure 4.2.2b, the 1st harmonic of the signature is found on both sides of the origin, where the top harmonic is indicated with a green box. The intensity of higher harmonics decreases rapidly with increasing harmonics order and are therefore not observed here in the frequency plane.
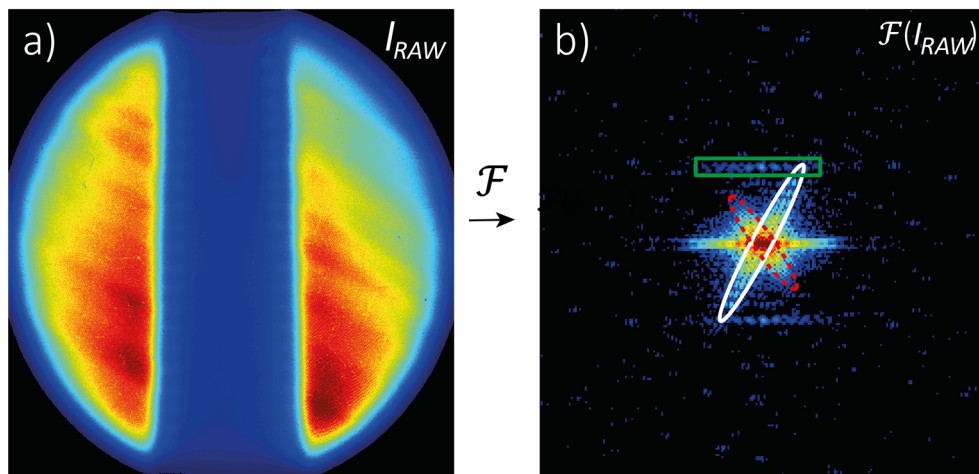
Figure 4.2.2. PFLIF image, shown in a), containing both naturally present OH and the frequency modulated OH fragments in the reaction zone. I_{RAW}, turned to the Fourier plane, is presented in b) where the green box denotes the 1st harmonics of the frequency modulated laser sheet, the white ellipse represents frequencies associated with the probe laser and noise from the camera is displayed as the red dashed ellipse.

In order to extract the desired OH fragment signal a band-pass filter was utilized in the post processing. This band-pass filter extracts all signals within the filter range and should be selected in such a way that unwanted frequencies are excluded. Due to the relatively large line-separation of the grating, the 1st harmonic ends up rather close to the origin. Increasing the modulation frequency also increases the distance between the harmonics and the origin in the Fourier plane. In the present study, we were, due to technical limitations, restricted to a 0.3 mm line separation and in order to exclude unwanted frequencies stemming from the probe-laser beam and the camera, these components were tilted with respect to the modulated pump-laser sheet. In Figure 4.2.2b the red dashed ellipse surrounds the camera noise, whereas signal from the probe laser beam is enclosed with the white ellipse. Due to the tilting, the interfering frequencies are positioned at a different location in the frequency plane, thereby minimizing signal crosstalk. To extract the signal from the OH fragments a band-pass filter, generated as an elliptical super Gaussian window, was employed to $\mathcal{F}(I_{RAW})$, frequency shifting to the origin, followed by inverse Fourier transformation and the result is depicted in Figure 4.2.3.
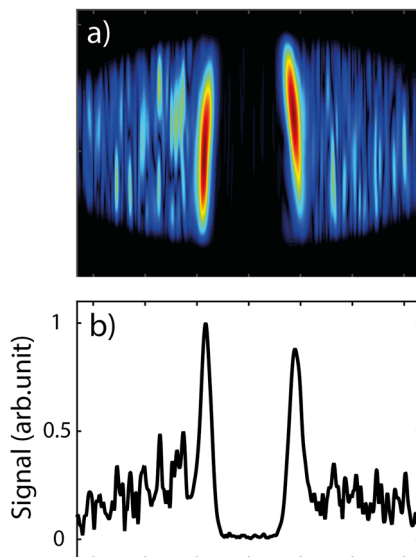
Figure 4.2.3. Extracted signal from I_{RAW} is presented in a), vertical integration of I_{RAW} is depicted in b). Here, residual structures of the probe laser beam are clearly seen next to the two peaks in the reaction zone.

As already mentioned, for this setup the pump- and probe laser sheets are only crossing in the reaction- and unburned zones of the flame, giving no OH fluorescence signal stemming from CO_2 photochemistry in the product zone. The signal in the product zone, seen in Figure 4.2.3, thus stems from signal crosstalk from the probe laser beam. The image in Figure 4.2.3a is the extracted image from I_{RAW} and Figure 4.2.3b is a vertical integration of the image displayed in Figure 4.2.3a. In order to further suppress the unwanted signal in the product zone a different approach was established, this time in the post-processing routine. A background image was extracted from I_{RAW} by multiplying $\mathcal{F}(I_{RAW})$ with an inverted super Gaussian band pass filter, suppressing the modulation frequency. Inversely Fourier transforming the modified $\mathcal{F}(I_{RAW})$ gives an image without the coded OH fragments, i.e. a background image I_{BKG}. Here, I_{BKG} contains all signal that does not have the same modulation frequency as the OH fragments, see Figure 4.2.4.
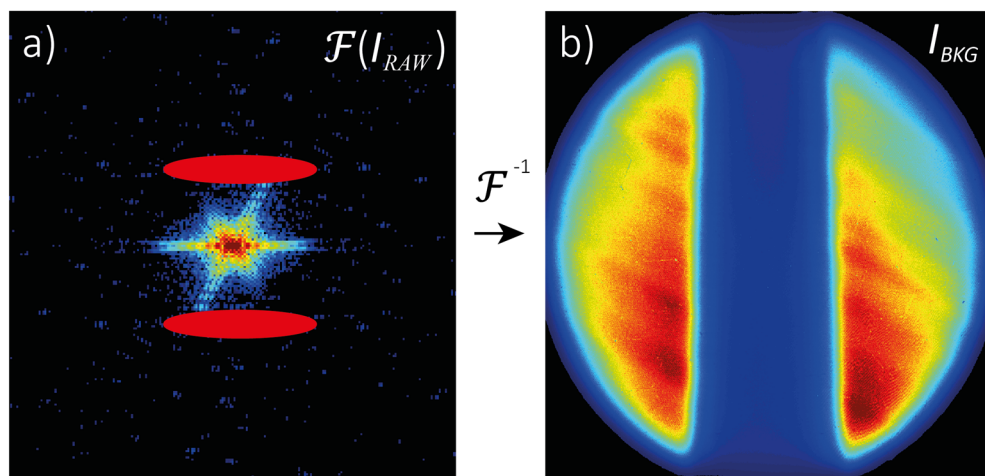
Figure 4.2.4. The inverted super Gaussian band-pass filter multiplied with $\mathcal{F}(I_{RAW})$ is illustrated in a) as the red filled ellipses. I_{BKG} is the result of an inverse Fourier transform of a) and presented in b).

Moreover, a self-compensated image, I_{SC}, was created by dividing I_{RAW} with I_{BKG}, leaving only the modulated OH fragments in the reaction zone, see Figure 4.2.5a. The Fourier transform of I_{SC}, $\mathcal{F}(I_{SC})$, is depicted in Figure 4.2.5b, where it is clearly seen that all unwanted frequencies are suppressed, compare with Figure 4.2.2b, whereas the 1st harmonic of the modulated OH fragments is enhanced.

Figure 4.2.5. A self-compensated image, I_{SC}, was constructed from the ratio I_{RAW}/I_{BKG} displayed in a). The Fourier transform of a), with the 1st harmonic of the modulated signal, displayed on both sides of the origin is presented in b).

Again, to extract the modulated OH fragment signal from I_{SC} the spatial frequency lock-in algorithm was utilized. A bandpass filter positioned at the desired modulation f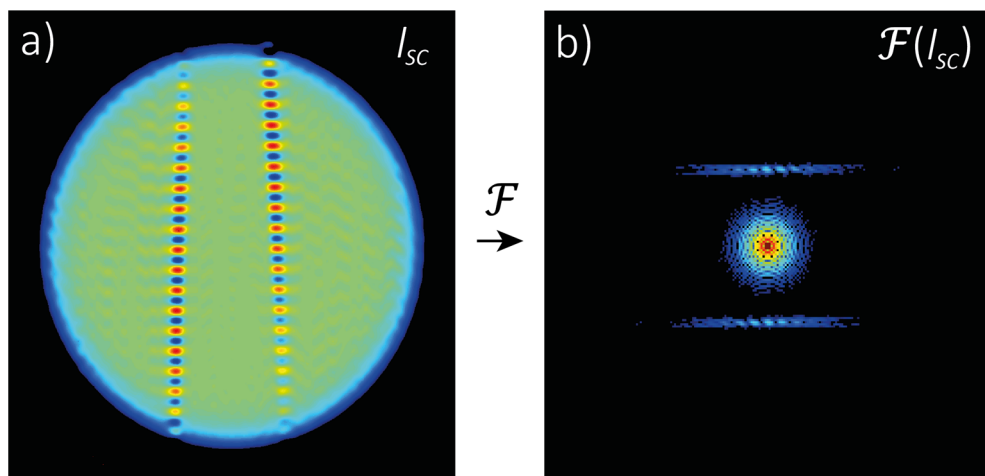requency was multiplied with I_{SC}, frequency shifted to the origin, inversely Fourier transformed and the final image was generated, I_{PFLIF}. The final image is shown in Figure 4.2.6, where 4.2.6a is I_{PFLIF} and the blue curve in 4.2.6b is a vertical integration of 4.2.6a. The displayed image is a single-shot image of hydrogen peroxides performed in a premixed laminar CH_4/air flame. The red line represents the intensity of the naturally present OH signal in I_{RAW}. Note, that the intensity scale is 25 times lower for the OH fragment signal than for the naturally present OH. It should be emphasized that all images and in particular the final image, I_{PFLIF}, are extracted from I_{RAW}.
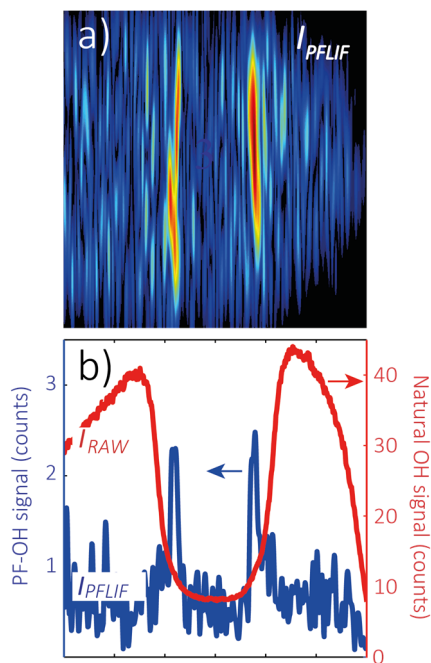
Figure 4.2.6. A single-shot image, I_{PFLIF}, of hydrogen peroxides in the reaction zone of a CH_4/air flame is presented in a), with vertical cross section of I_{PFLIF} as the blue curve in b). The red curve in b) represents the naturally present OH signal in the flame.

When combining PFLIF and SI, only one image has to be acquired for 2D imaging of hydrogen peroxides in a premixed hydrocarbon flame and hence, the concept opens up for single-shot measurements in non-stationary environments. Imaging of hydrogen peroxides in turbulent flames will, however, be challenging due to the aforementioned chemically produced OH radicals upon CO_2 photolysis. The production of these OH fragments will be discussed in the next section.

4.3 Picosecond laser pulses for flame diagnostics

In the work presented in Paper III, the chemically produced OH in the reaction- and product zones of a CH_4/air flame have been investigated for both nanosecond and picosecond laser pulses. Data of nanosecond laser pulses from Johansson *et al.* [1], illustrating the time dependence of the OH signals are depicted in Figure 4.3.1. The left graph illustrates the time-dependent product zone signal, while the right graph represents the signal in the reaction zone.

To suppress the interfering OH signal in the product zone pump-probe delay time studies ranging between 0.5- and 22.5 ns were carried out. It was found that virtually the entire interfering signal in the product zone was suppressed for delay times shorter than 2 ns. It was, however, also found that for delay times below 5 ns a prompt diffuse signal appears in the reaction zone that needs to be subtracted. It is interesting to note that the OH signal in the reaction zone increases with time delay and reaches a maximum at 200 ns. This has been investigated further in Paper III, where a chemical model describing the OH production in the reaction zone is presented.
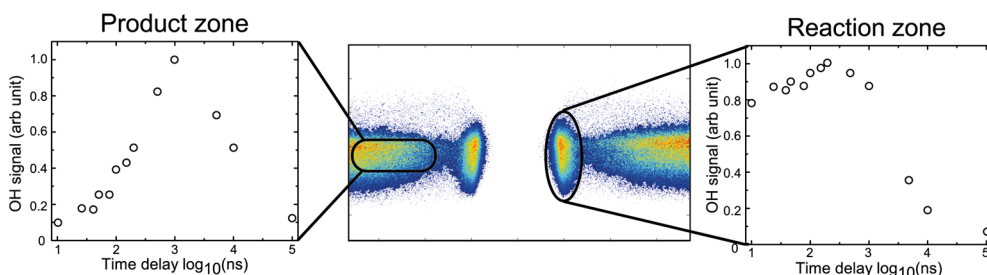
Figure 4.3.1. The pump-probe delay time dependence of OH production in the reaction- and product zones. The figure is adapted from data presented by Johansson et al. [1]. The left graph shows the time dependence of the product zone signal with a maximum at 1000 ns, while the right graph presents the time dependence of the reaction zone signal with a maximum at 200 ns.

4.3.1 OH production in the product zone

The OH production in the product zone, mainly stemming from photolysis of hot CO_2 was investigated for delay times between 0.5- and 22.5 ns and compared with data points acquired by Johansson *et al.* [1]. The result is depicted in Figure 4.3.2, where the black circles and red squares are data points from nanosecond and picosecond laser pulses, respectively. The data points coincide rather well with the calculation performed by Johansson *et al.*, but the initial picosecond data points form a steeper gradient than the calculated curve. One possible explanation is that the calculation assumes that 10% of the CO_2 molecules forms CO and $O(^3P)$, which was the case for nanosecond laser

pulses. For picosecond laser pulses the irradiance was higher and 25% of the CO_2 was estimated to be photodissociated (calculated from Equation 1 in [1]). Also, $O(^1D)$ may be formed, thus increasing the OH production rate.
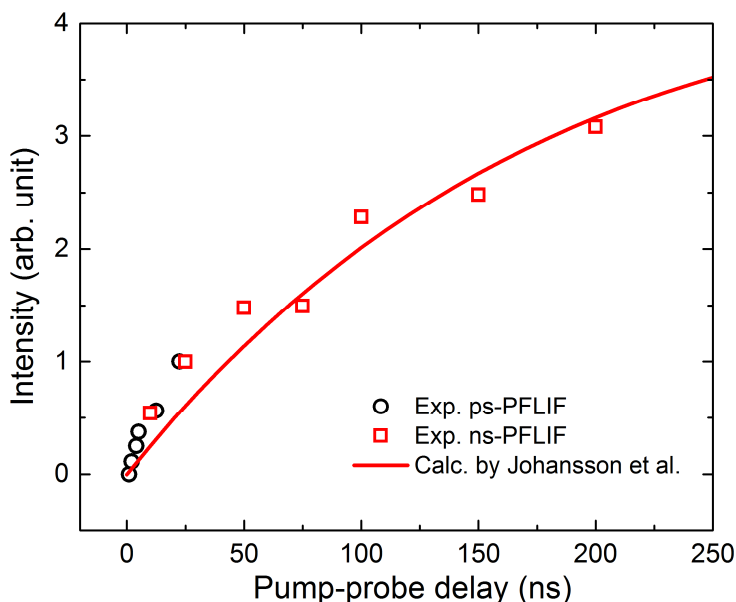
Figure 4.3.2. Production of OH in the product zone, where the black circles are data from picosecond laser pulses, whereas the red squares are data points from nanosecond laser pulses found in Johansson et al. [1].

4.3.2 OH production in the reaction zone

The OH production in the reaction zone upon photolysis of HO_2 is dependent on; photolysis wavelength and irradiance. A model predicting the photochemical production of OH in this region is described in detail in Paper III, and below follows only the final expression for OH production in the reaction zone with the same indices as in Paper III.

$$\frac{[OH](t)}{[OH]_0} = (1-x)\left(2 - e^{-k_{eff}^P \cdot t}\right)$$
$$+ x\left(\left[1 + \frac{k_0^D}{k_{eff}^D}\left(1 - e^{-k_{eff}^D \cdot t}\right)\right] + \frac{k'}{k_{eff}^D}\left(1 - e^{-k_{eff}^D \cdot t}\right)\left(1 - e^{k_2' \cdot t}\right)\right).$$

$$(4.3.1)$$

Here, the variable x ($0 \leq x \leq 1$) is designated to the $O(^1D)/O(^3P)$ branching ratio so that x = 1 represents 100 % $O(^1D)$ and 0 % $O(^3P)$, whereas x = 0 means 100 % $O(^3P)$ and 0 % $O(^1D)$. In the work presented in Paper III OH production for different branching ratios are predicted for a stoichiometric, i.e $\varphi = 1$, CH_4/air flame, while Figure 4.3.3 shows the corresponding analysis for a leaner, $\varphi = 0.6$, and a richer, $\varphi = 1.6$, flame. It can be seen in Figure 4.3.3a that the OH production is insignificant during the first 200 ns when only $O(^3P)$ is formed, i.e. for x = 0 for the lean flame. Both the lean- and the rich flames exhibit steep initial OH buildups for x ≥ 0.2, but the behavior for t > 20 ns is quite different for the lean and the rich flame. For the lean flame the curves are all essentially flat beyond 20 ns, while the OH concentration continues to increase linearly for the rich flame, where the slope decreases for increasing branching ratio. The reason for the varying behavior probably depends on that the water concentration for the lean flame is about ten times higher than the methane concentration in the reaction zone, whereas for the rich flame these concentrations are similar. Having this in mind, gives an OH buildup that is about ten times faster for the rich flame than for the lean flame, which for the lean flame leads to a rather flat slope beyond 20 ns for the short time interval displayed in Figure 4.3.3.
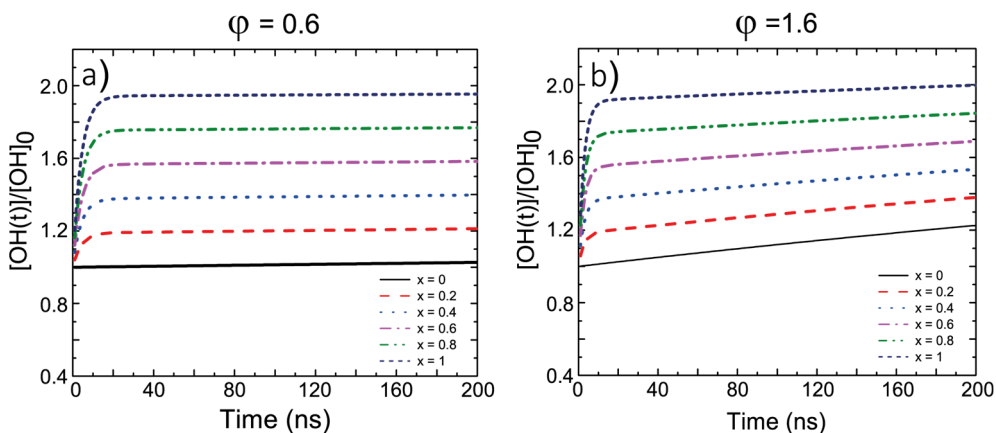
Figure 4.3.3. Branching ratio of $O(^1D)/O(^3P)$ for a) $\varphi = 0.6$ and b) $\varphi = 1.6$. At x = 0, 100% $O(^3P)$ is formed and at x = 1, 100% $O(^1D)$ is produced.

4.4 Imaging of hydrogen peroxides in turbulent flames

The presented studies have been demonstrated in laminar flames, in which single-shot imaging is not necessary for diagnostics purposes. However, most practical applications such as turbulent flames requires single-shot imaging. The SI-PFLIF technique opens up the possibility to employ single-shot measurements in non-stationary environments,

but has a challenge in discriminating OH fragments that are produced by the pump laser. For hydrocarbon flames both OH signal stemming from hydrogen peroxides and hot CO_2 are intensity modulated, whereas for hydrogen flames, lacking CO_2, all OH fragments stem from hydrogen peroxides. Single-shot imaging of hydrogen peroxides, using the SI-PFLIF method, will thus be possible in hydrogen flames.

Using picosecond laser pulses allow drastic shortening of the pump-probe delay time and thereby suppression of virtually the entire photochemical interference. However, the high laser peak power and the short delay required to maximize the suppression give rise to new challenges, namely production of extremely reactive $O(^1D)$ radicals, due to multi-photon dissociation, and the need to subtract a diffuse signal promptly produced in the reaction zone (for delay times shorter than 5 ns). The prospect of SI-PFLIF based on picosecond laser pulses for interference free single-shot imaging of hydrogen peroxides in turbulent hydrocarbon flames thus appear limited.

For single-shot turbulent flame diagnostics in hydrocarbon flames, the best choice would rather be to employ the SI-PFLIF concept with nanosecond laser pulses, keeping the pump-probe delay time as short as possible. Nevertheless, the prompt signal in the reaction zone induced by the pump beam has to be suppressed, which is achieved at delay times longer than 5 ns. In addition, at delay times longer than 5 ns signal from OH fragments originating from CO_2 photolysis is significant and may not be separated from OH fragments stemming from hydrogen peroxides. In turbulent flames the reaction- and product zones are not well-defined and thus imaging of hydrogen peroxides are expected to be challenging. One should also bear in mind that any potential signal contribution from interfering frequencies induced by e.g. the probe laser or the camera such as in Figure 4.2.3 has to be clarified and not mistaken for OH fragment signal.

Nevertheless, for conditions, such as equivalence ratio, pump-probe wavelengths and fluence, i.e. the laser sheet area and the laser pulse energy, used in Johansson *et al.* [1], a pump-probe delay time of 5 ns gives an OH fragment signal stemming from hydrogen peroxides that is roughly 10 times stronger than the photochemically produced OH signal originating from CO_2. If all conditions are selected in such a way that the OH fragment signal stemming from hydrogen peroxides is maximized compared to the photochemical OH signal, a larger ratio between the two OH signals may be achieved. For instance, Malin Jonsson has in her Doctoral thesis [45] investigated how the fluence, influences the ratio ($N_{OH(HO2)}/N_{OH(CO2)}$) and found that the HO_2 signal is favored by a lower fluence. In addition, she also found that there is a trade-off between minimizing the CO_2 interference and maximizing the signal from hydrogen peroxides. The work presented in this chapter has mainly focused on stoichiometric CH_4/air flames in which the hydrogen peroxide concentration is rather low. If the fuel is changed from methane to dimethyl ether, DME, the hydrogen peroxide number density is increased by a factor of two.

In conclusion, for hydrogen peroxide imaging using SI-PFLIF in turbulent flames, the best choice would be to use hydrogen flames in which CO_2 is absent. However, if

all conditions are maximized so that the OH signal stemming from hydrogen peroxides is high compared to the photochemical OH signal from CO_2, imaging in turbulent hydrocarbon flames may be possible.

Chapter 5

Plasma studies

The present chapter will review Paper V-VII. Ozone imaging in an ozone flow under ambient conditions and a gliding arc discharge will be discussed followed by NO_2 LIF measurements in an industrial test rig at Tetra Pak Packaging Solutions AB. Prior to the presentation of the papers, some basic aspects of plasma spectroscopy is discussed. Plasmas produced by either the gliding arc discharges or electron beam in the test rig produces electrons having energies that vary several orders of magnitude. For the gliding arc discharge the kinetic energy of the electrons are roughly 0.8 eV [17], whereas the test rig was operating with electrons of 100 keV.

5.1 Introduction to plasma spectroscopy

Plasma is the fourth state of matter after, solid, liquid and gas and is in its simplest form an ionized gas in which electrons, ions and neutral atom and molecules are enclosed in electromagnetic fields [46]. There are two major types of plasmas, namely thermal and non-thermal ones. In thermal plasmas the neutral molecules and ions have the same temperature, while in non-thermal plasmas supplied energy is transferred to electrons and thereby increases their temperature, which leads to a higher electron temperature compared to the molecular- and ion temperatures [47]. Pulsed microwaves [48] or nanosecond high-voltage pulses [49] may for example form non-thermal plasmas. Also, the two plasmas treated in this work, produced by either the gliding arc discharge or the electron beam, are both non-thermal, but due to the drastic difference in electronic energy, their compositions are substantially different. Figure 5.1.1 shows the two experimental setups used to study the two different plasmas, where Figure 5.1.1a shows the gliding arc setup and Figure 5.1.1b depicts the electron beam rig. As can be seen the two plasmas visually look very different. For the gliding arc discharge an electric current is passing through two electrodes and a plasma is produced. The electrodes are positioned above a tube typically issuing a flow of air. A detailed description of the

gliding arc discharge can be found in the thesis by Jiajian Zhu [18]. For the electron beam setup a plasma is created as highly energetic electrons are accelerated through a vacuum pipe and propagate through a thin foil before interacting with ambient air.
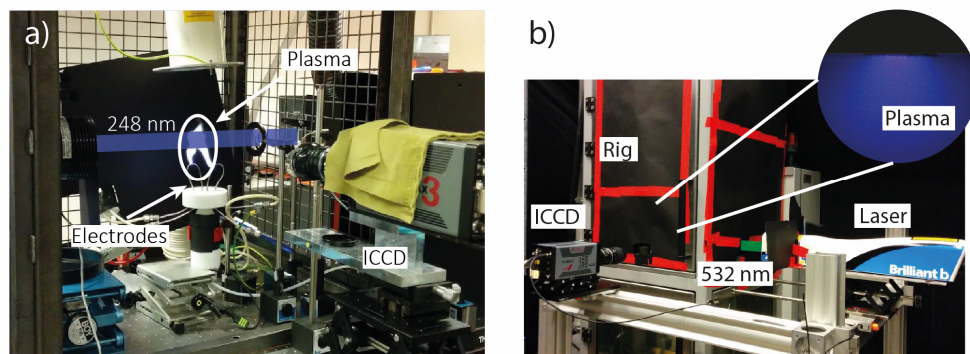

Figure 5.1.1. The two different types of plasmas studied in this thesis project, gliding arc discharge is presented in a) and electron beam is shown in b). Some important components are pointed out for each setup and the laser beams are illustrated as blue, 248 nm, or green, 532 nm, lines.

To characterize non-thermal plasmas, various optical diagnostic tools may be utilized [50]. For instance, optical emission spectroscopy, OES may be used to determine translational- and vibrational temperatures [51–53], while the density and distribution of reactive species, such as OH, may be studied using LIF [54,55]. Essentially, Laser Thomson scattering, LTS, is elastic scattering of a photon interacting with an unbound free electron and may be used to study electron temperature and density [56]. For the plasma produced by electron beam, LIF has in this work been employed to measure NO_2, while PFLIF has been used to image O_3 produced by the gliding arc discharge.

5.2 Ozone imaging under ambient conditions

Details concerning ozone imaging in an O_3 flow under ambient conditions are found in Paper V. The reader is also referred to the photophysics chapter, 2.2, for a thorough description of PFLIF applied for ozone detection as well as vibrational population distributions of the hot O_2 fragments. This section will briefly discuss the major conclusions regarding O_3 imaging, using the PFLIF concept with a 248 nm laser beam.

Detection of O_3 using a one-pulse PFLIF configuration have previously been carried out by Pitz *et al.* [57] in tagging velocimetry measurements. In Paper V, the focus was to investigate the potential of O_3 imaging using PFLIF, paving the way for forthcoming applications such as studies of plasma assisted combustion, PAC.

A major product channel for ozone photolysis by 248 nm is formation of $O(^1D)$ radicals which are extremely aggressive and react rapidly with species such as H_2O and CH_4. A study was carried out in a reactor supplied with a preheated mixture of $CH_4/air/O_3$ and the result is presented in Figure 5.2.1. The gas temperature was varied, while the O_2 fluorescence stemming from O_3 was captured by both a spectrograph and an ICCD camera. As the temperature increases O_3 decomposes into O and O_2 leading to a lower ozone concentration in the probe volume. It was concluded that merely O_2 emission stemming from O_3 was captured on both devices since the circle- and cross data points in Figure 5.2.1 overlaps rather well. Ozone imaging using PFLIF may thus be feasible in this kind of environment. One of the major challenges with ozone imaging in PAC is the influence of naturally present vibrationally hot O_2. This aspect has been investigated in detail in a gliding arc discharge and is presented in the next section.
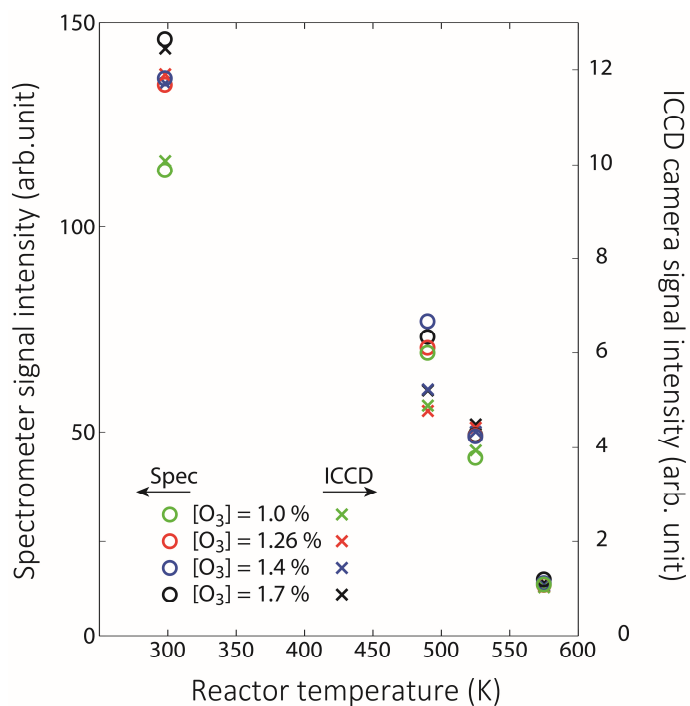

Figure 5.2.1. A spectrograph and an ICCD camera were simultaneously capturing O_2 fluorescence stemming from O_3. The temperature in the probe volume was varied between 300- and 575 K in the reactior supplied with a gas mixture of $CH_4/air/O_3$.

5.3 Ozone imaging in a gliding arc discharge

This section concerns experiments conducted in the work presented in Paper VI, in which the reader will find all details regarding the study. A photograph of the experimental setup for the gliding arc discharge is found in Figure 5.1.1a, where the 248 nm beam is illustrated as the blue horizontal line. Experiments were conducted for three measurement cases, case I-III, which are illustrated in Figure 5.3.1. To the left schematics of the experimental setups are shown, while the lifetime of either hot O_2 or ozone is presented for each case to the right. For case I and II the pump- and probe processes were separated by two different laser pulses, 266 nm and 248 nm, respectively. This configuration allowed pump-probe delay studies, in which the 266 nm pump pulse dissociated O_3 into O and hot O_2 fragments, while the 248 nm probe pulse electronically excited the hot O_2 fragment at delay times ranging between 10- and 10^5 ns. The pump-probe delay studies were carried out in both a laminar ozone flow (case I) and in ozone produced by the gliding arc discharge (case II). In case III only the 248 nm laser was operating, thus acting as both pump- and probe beam. The lifetime of ozone produced by the gliding arc discharge was studied by turning off the discharge prior to the arrival of the 248 nm pulse. The delay between the turn off of the discharge and the 248 nm pulse was ranging from 0.5- to 5 ms. The lifetime of vibrationally hot O_2 in the O_3 flow (case I) and in ozone produced by the gliding arc discharge (case II) was determined to be on the nanosecond scale, whereas the lifetime of ozone produced by the gliding arc discharge (case III) was on the order of milliseconds.

Furthermore, the fact that hot O_2 has such short lifetime compared to ozone produced by the gliding arc discharge, strongly justifies monitoring of ozone by applying PFLIF several microseconds after the gliding arc discharge is turned off. In addition, the probability that chemical reactions will produce significant amount of hot O_2 is very low such a long time after the high voltage is turned off. The data points for case II and III were acquired when the discharge was turned off to ensure that the electron density was low enough to prevent direct formation of hot O_2 or other species that through chemical collisions could produce hot O_2 [58]. However, the amount of naturally present hot O_2 in the gliding arc discharge was estimated to be several orders of magnitude lower than hot O_2 generated from photolysis of O_3 and hence O_3 may be imaged when the gliding arc discharge is operating.
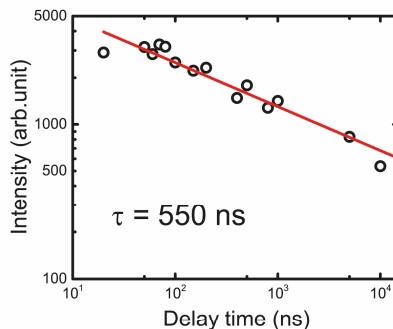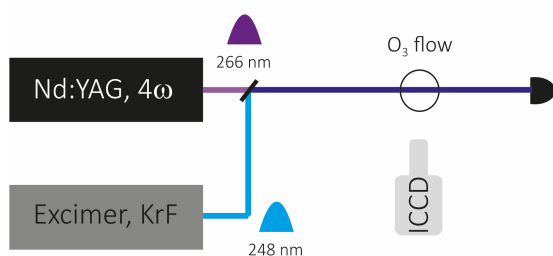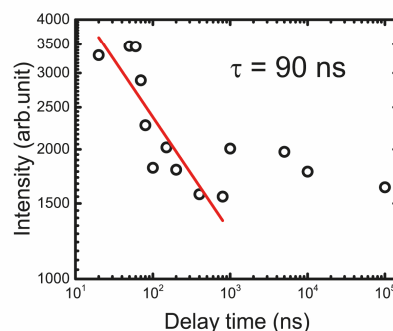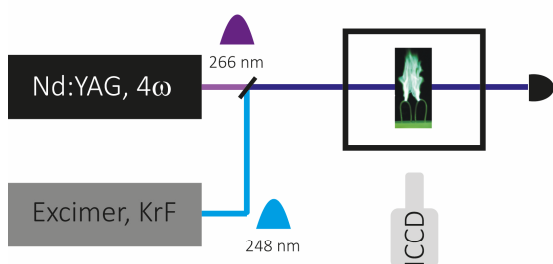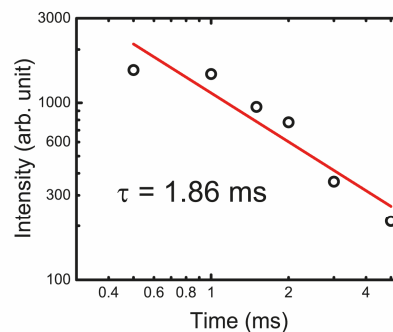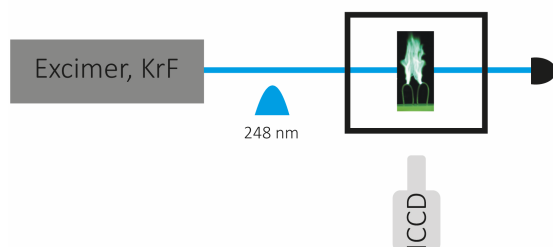
Figure 5.3.1. The three measurement cases, I, II and III are illustrated to the left, while the result for each case is presented to the right. It was found that the lifetime of hot O_2 (case I and II) is several orders of magnitude shorter than the lifetime of ozone produced by the gliding arc discharge (case III)

Figure 5.3.2 shows single-shot images of O_3 recorded in the gliding arc discharge. The images were recorded with the 248 nm laser beam operating and an input power to the discharge of 400 W with an air flow kept at 15 l/min. Ozone has a rather long lifetime (~2 ms) and may therefore be found in wide areas outside the plasma column, which is

clearly seen in both Figure 5.3.2a and b. As pointed out in Figure 5.3.2a the plasma column is located in the bottom center of the images.
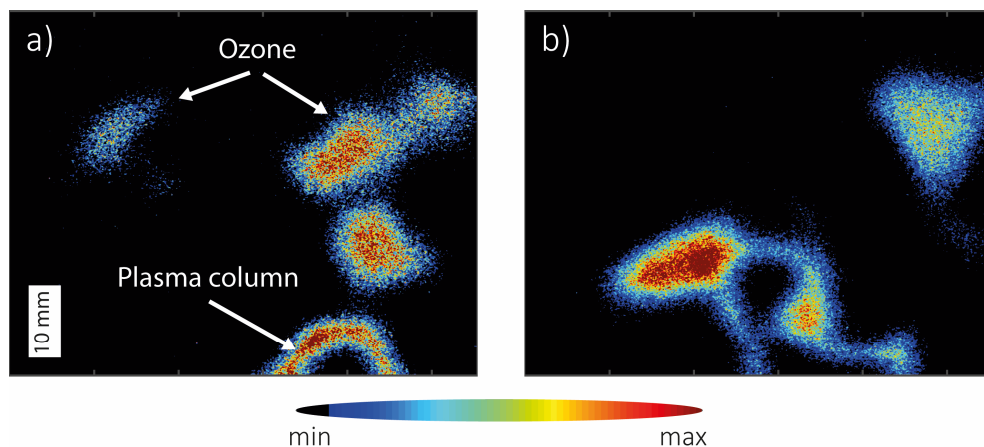
Figure 5.3.2. Single-shot images of O_3 in the gliding arc discharge. The plasma column is located as a string in the bottom center of the images, while ozone is distributed in rather wide regions outside of the plasma column.

5.4 Study of NO_2 in a sterilization rig

In the work presented in paper VII, NO_2 LIF images were recorded of a plasma produced by electron beam at Tetra Pak. The setup is shown in Figure 5.1.1b, where the plasma is found behind the black sheets covering the rig. The plasma emission was captured by an optical fiber coupled to an Ocean optics USB spectrograph. The total spectrum is depicted in Figure 5.4.1a and merely visualizes emission peaks from the 2nd positive system of N_2(C-B), with small contributions from N_2^+(B-X). The graph in Figure 5.4.1b is a zoom in between 600- and 800 nm, illustrating the 1st positive system of N_2 and is indicated by the red dashed box in Figure 5.4.1. The rig operates under ambient conditions in air and thereby has a nitrogen concentration of ~78%. It is therefore not surprising that the emission spectrum is dominated by N_2 and N_2^+, since the high electron energy (~100 keV) excites most of the species in the probe volume. Oxygen emission is not seen in Figure 5.4.1, which likely is a result of that most oxygen emission is present in the UV regime [59], where the spectrograph was not sensitive.

Figure 5.4.1. Plasma emission produced by electron beam. In a) is the total plasma emission shown and in b) is a zoom-in between 600- and 800 nm presented.

To study NO_2 in the plasma, laser-induced fluorescence was used and 532 nm laser pulses were propagating through the plasma to induce fluorescence from NO_2 between 550- and 900 nm [60]. In addition, Monte-Carlo simulations were performed at Tetra Pak in order to determine the electron dose distribution (dose is energy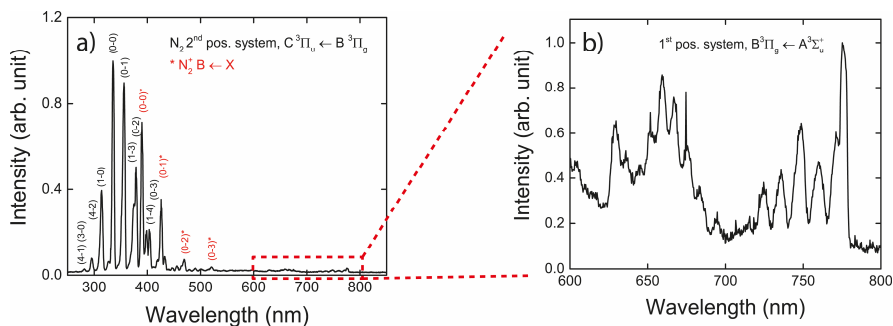/mass in unit [J/kg]). These results were compared and are shown in Figure 5.4.2. Figure 5.4.2a and Figure 5.4.2b are the NO_2 and electron dose distributions, respectively, along a horizontal line at different distances from the emitter, while Figure 5.4.2c and Figure 5.4.2d displays how the NO_2 concentration varies with electron energy for experiment and simulation, respectively. For reasons of clarity, the plasma emission captured with an ICCD camera is presented in Figure 5.4.2e, where the vertical distance 0 indicates the point at which the electrons interact with air and the horizontal distance 0 indicates the center of the emitter.

   Although, no detailed analysis of the electron dose and NO_2 concentration have been carried out, it is clearly seen in Figure 5.4.2 that there are similarities. In Figure 5.4.2a and Figure 5.4.2b the slope of the curves closer to the emitter is steeper than the curves further away from the emitter. In addition, the shapes of the curves for the experimental and simulated data agree well and thereby indicating that there is a relation between NO_2 concentration and electron dose. Moreover, in Figure 5.4.2c and Figure 5.4.2d the NO_2 concentration was measured and the electron dose was simulated for varying electron energy and the result is similar for both the experimental and simulated data points. The highest NO_2 concentration and electron dose distribution was obtained at the lowest electron energy, while the slopes representing a shorter distance to the emitter have a larger gradient. The reason that the NO_2 concentration is lower further away from the emitter most likely depends on that the electron density and the electron energy are lower and thereby the probability that chemical reactions will form NO_2 is decreased. The concentration of NO_2 was measured to range between 10- and 100 ppm in the plasma depending on position and operating rig conditions, which is in the same order as measured by gas analysis at Tetra Pak.

The possibility of measuring O_3 in the plasma will be treated in the outlook in section 6.2.1.
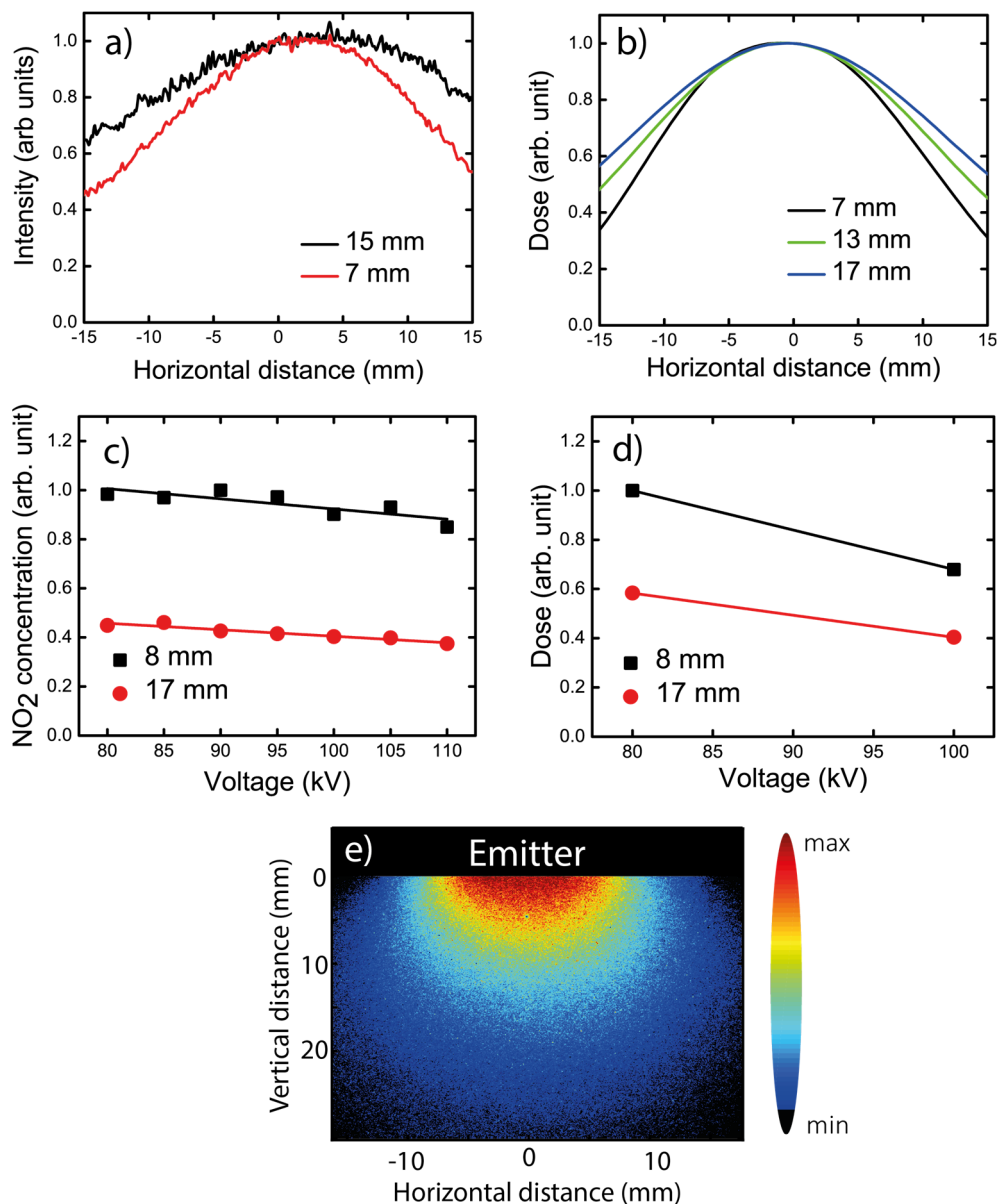

Figure 5.4.2. Experimental data compared to simulations for different parameters. In a) and b) are experiments and simulations shown, respectively, compared with horizontal distance under the emitter. In c) and d) are experiments compared to simulations presented, respectively, for different electron energies and the plasma emission captured on an ICCD camera is found in e).

Chapter 6

Summary and outlook

The present chapter will give a brief summary of the major conclusions that were found in this thesis project together with suggestions for further studies aiming to improve the presented techniques. In the flame studies, one of the goals was to extend the PFLIF technique to be applicable in turbulent flames, while characterization of the plasmas has been the main focus in the gliding arc discharge and electron beam applications. Ideas for further studies in plasmas and diagnostic approaches towards species-specific measurements of hydrogen peroxides will be discussed as well.

6.1 Summary and conclusion

This thesis project has included three different measurement environments namely, flows of vaporized H_2O_2/H_2O, a premixed hydrocarbon flame and plasma produced by either a gliding arc discharge or electron beam. Except for NO_2 imaging in the plasma produced by electron beam, PFLIF has been employed in all measurement environments.

In Chapter 3, simultaneous imaging of H_2O_2 and H_2O using two different measurement concepts were presented and discussed. In one of the concepts PFLIF, for imaging of hydrogen peroxide, was combined with tp-LIF for water vapor visualization. A pump-pulse dissociates H_2O_2 into two OH fragments, whereupon a second laser pulse probed the OH fragments. The pump-pulse wavelength was selected in such a way that simultaneous absorption of two photons electronically excited the water molecule and the subsequent fluorescence was detected. Predissociation, where one OH fragment is formed, is the dominant loss factor for the H_2O fluorescence. It was found that the signal intensity of this OH fragment was insignificant compared to OH fragments generated by photolysis of H_2O_2 and hence all detected OH emission can be assumed to originate from H_2O_2.

The other concept utilizes the spectral and temporal shape of OH fluorescence stemming from hydrogen peroxide to extract both water and hydrogen peroxide mole fractions. The concept is based on the fact that collisions with water molecules influence the spectral/temporal distribution of the OH fluorescence. The total fluorescence reflects the hydrogen peroxide concentration, while the ratio between emission bands or different temporal regimes can be used to extract the water vapor concentration. The sensitivity of the technique is increased if the vaporized H_2O_2/H_2O mixture is surrounded by a bath gas that has low cross section for collisional quenching, and therefore argon was employed as bath gas.

Two studies of hydrogen peroxides in premixed laminar hydrocarbon flames were presented in Chapter 4. Here, structured illumination was combined with PFLIF to suppress signal from naturally present OH radicals and perform single-shot measurements in flames. The pump beam was spatially intensity modulated by a transmission grating, and thereby the generated OH fragments, stemming from manly HO_2, were formed with a recognizable pattern upon photolysis. The probe beam excites both the OH fragments and the naturally present OH in the flame, and the induced fluorescence was captured by an ICCD camera. The desired OH fragment signal was extracted by transforming the recorded image into the frequency plane and then utilizing a post-processing routine. Furthermore, in the second study PFLIF measurements with picosecond laser pulses were carried out in order to minimize the influence of chemically produced OH radicals, originating from CO_2 photolysis, in the product zone. In addition, a chemical model was developed to simulate the OH production in the reaction zone, which revealed that OH not only is formed promptly through HO_2/H_2O_2 dissociation, but is also accompanied by a very rapid buildup through reactions with $O(^1D)$ fragments stemming from HO_2 photolysis. The model also allowed determination of the $O(^3P)/O(^1D)$ branching ratio.

In Chapter 5, ozone imaging using PFLIF was presented in a laminar ozone flow and in a plasma produced by a gliding arc discharge. A preceding pump beam photodissociates O_3 into O and vibrationally hot O_2 fragments, whereupon the probe beam electronically excites the hot O_2 fragment and the resulting fluorescence is collected and detected by an ICCD camera. The plasma, produced by the gliding arc discharge, generates vibrationally hot O_2 and a study aiming at measuring the lifetimes of ozone and vibrationally hot O_2 was conducted. It was found that the lifetime of ozone was several orders of magnitude longer than the lifetime of vibrationally hot O_2. In addition, the concentration of naturally present hot O_2, produced by the gliding arc discharge was estimated to be minor compared to the amount of hot O_2 formed by photolysis of O_3. It was concluded that ozone can be visualized using PFLIF in a plasma produced by an operating gliding arc discharge that generates electrons with a kinetic energy of ~0.8 eV. Studies of ozone in other type of plasmas, for which naturally present hot O_2 can not be neglected, requires that the plasma production is turned off prior to the arrival of the pump pulse.

Finally, NO₂ LIF measurements were carried out in a plasma, produced by electron beam, in a sterilization rig at Tetra Pak. The NO_2 LIF distributions at several distances from the emitter were compared with electron dose simulations. It was found that there is a correlation between measured NO_2-LIF signal and the electron dose simulations. However, it was also concluded that further investigations need to be carried out to fully understand the relation between the electron dose and the NO_2 distribution.

6.2 Outlook

6.2.1   Plasma diagnostic

Ozone imaging in a plasma using PFLIF with 248 nm laser pulses requires that the signal from naturally present vibrationally hot $O_2(v'' = 6, 7)$ is low enough not to interfere with the signal from the vibrationally hot $O_2(v'' = 6, 7)$ fragments stemming from photolysis of O_3. One way to improve the selectivity is to temporally separate the pump from the probe process and photodissociate O_3 into O_2 fragments that populate higher vibrational states which then can be probed by a second laser pulse. For instance, photolysis with 240 nm laser pulses puts substantial population in $v'' = 14$ [31], which may be probed at ~364 nm [25].

The main limitation with laser diagnostics in the electron beam rig at Tetra Pak was the optical access, which was lead-seeded glass and thus measurement in the UV-region was not an option. The highly energetic electrons produce ionizing radiation and thus lead-seeding is required, but replacing the glass with quartz would allow studies of species absorbing/emitting in the UV-regime. In the work presented in Paper VII, the consumption of NO_2 was analyzed when the emitter was turned off and a rough estimate of the ozone concentration, based on very simplified kinetics, indicated ~1.5 % ozone in the plasma produced by the electron beam. An optical access transmitting UV light would allow ozone imaging in the plasma by PFLIF, as described in Chapter 5.3. At the electron energies prevailing in the test rig, i.e. 100 keV, the concentration of hot O_2 at $v'' = 6, 7$ is expected to be significant and may not be separated from hot O_2 stemming from PFLIF of O_3. However, if the emitter is turned off the electron density is low enough within a couple of microseconds [58] to chemically produce hot O_2 and thus allowing for O_3 imaging in the rig. In addition, UV optical access to the rig allows for measurements of other intermediate species of great interest, such as OH, via LIF at 283 nm [54,61], and NO, by LIF at 226 nm [62].

It would also be of significant interest to measure the gas- and electron temperature in the plasma produced by the electron beam, which can be accomplished by Rayleigh and Thomson scattering. Thomson scattering is light scattering from free charges such as electrons and provides a Doppler broadened spectrum that is related to the electron

motion. The scattering spectrum provides information about electron density and electron temperature [63,64], see Figure 6.2.1a. When the electron velocity distribution is Maxwellian, the spectrum obtained by Thomson scattering is Gaussian and has a FWHM (full width at half maximum) that is proportional to the electron temperature. In addition, the total Thomson scattering intensity is directly proportional to the electron density [65]. Rayleigh scattering is light scattering from heavier species such as molecules and ions. The major difference between Rayleigh and Thomson spectra is illustrated in Figure 6.2.1b, which shows that Thomson scattering covers a broader wavelength range than Rayleigh scattering.
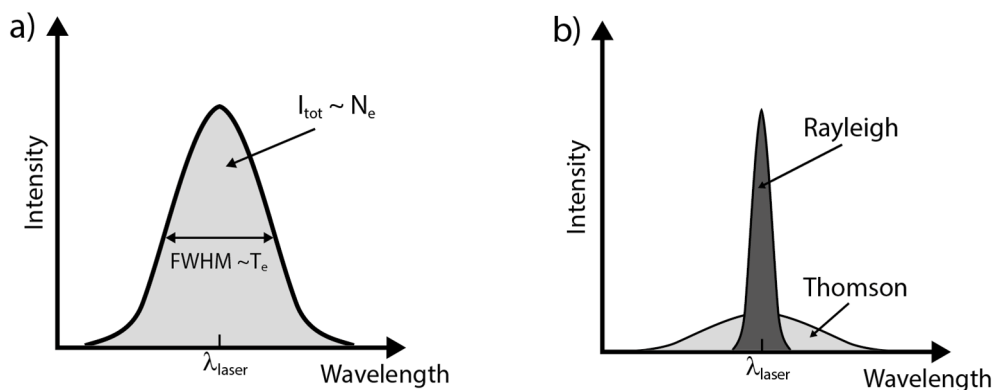
Figure 6.2.1. Schematic illustration of Thomson scattering spectrum is shown in a), where λ_{laser} is the laser source wavelength, T_e the electron temperature and N_e the electron density. The difference between Rayleigh and Thomson scattering spectra is presented in b).

Reactive species are formed when the highly energetic electrons interacts with ambient air in the rig. It would be of great interest to vary the chemical composition of the gas in the rig and simultaneously monitor the reactive species concentrations. Such a configuration would open up the possibility to minimize formation of undesired species.

6.2.2 Diagnostics for hydrogen peroxides

One of the major challenges with the PFLIF technique is that it is not species specific *per se*. In the flame studies presented in Chapter 4, the OH fragments generated upon photolysis of manly HO_2 and CO_2 were merely separated spatially by the product- and reaction zones in the laminar flame. A concept based on electronic excitation to a resonant state would therefore open up the possibility to solely detect HO_2 in the flame. In the literature it can be found that HO_2 has a low-lying bound electronic state, $1\,^2A'$, situated 0.76 eV above the ground state X^2A'' [37,66]. To the best of my knowledge

laser excitation to the 1^2A' state has not been reported. Instead, chemical reactions with manly oxygen molecules have been used to electronically excite the HO_2 radical into the 1^2A' state. However, it should in principle be possible to use a laser that emits between 1430 and 1510 nm to electronically excite the HO_2 radical to the bound $1^2A'$ state [67]. In addition, emission between 1430 and 1510 nm have been observed for the $HO_2(1^2A' \leftarrow X^2A'')$ band by Becker *et al.* [68] and, with higher resolution, by Tuckett *et al.* [69]. Provided that the laser beam is transformed into a sheet and a camera that is sensitive in the near-infrared region is available, selective 2D-visualization of HO_2 can potentially be achieved by LIF.
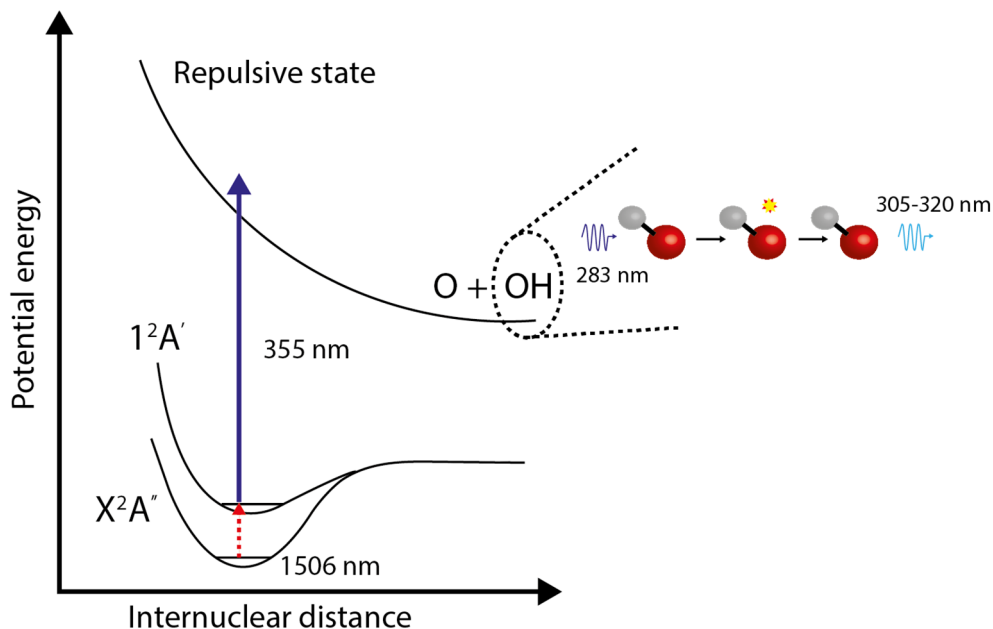
Figure 6.2.2. Schematic illustration of the three step concept for HO_2 visualization. A laser pulse, tuned to an absorption line of the $HO_2(1^2A' \leftarrow X^2A'')$ band at ~1506 nm is intensity modulated (illustrated as the dashed line) and used to electronically excite HO_2 to the 1^2A' state. The excited HO_2 is then photodissociated by a pump pulse (~355 nm) into two fragments, OH and O, whereupon the OH fragment is excited by a probe pulse (~283 nm) and the subsequent fluorescence (305-320 nm) upon relaxation is detected. If the IR pulse is not intensity modulated, the pump-pulse has to be selected in such a way that merely the excited HO_2 are dissociated and not other species that also could form OH radicals.

Furthermore, an additional idea for HO_2 visualization is to combine electronic excitation with PFLIF, see Figure 6.2.2. In such a configuration a laser pulse at roughly 1500 nm would first electronically excite HO_2 to the 1^2A' state, whereupon a second laser pulse at roughly 355 nm would photodissociate $HO_2(1^2A')$ into two fragments, OH and O. The OH fragment can then be probed by a third laser pulse at ~283 nm,

whereupon the subsequent OH fluorescence is monitored. In hydrocarbon flames, the presented concept may suppress the signal interference from OH radicals, stemming from hot CO_2, since the absorption cross section for CO_2 at ~2000 K is reduced by a factor of 10 for 355 nm photolysis compared to 266 nm laser pulses, which have been used in this thesis work [70]. In addition, if the first laser pulse is spatially intensity modulated, the concept opens up the possibility to perform single shot measurements of HO_2 in hydrocarbon flames since a post-processing routine can extract the OH fragments stemming from HO_2 photolysis in a similar manner as in the work presented in Paper IV. The intensity modulation of the first laser pulse also allows the concept to be species-specific since only HO_2 will be excited by the intensity modulated laser pulse.

Although, in principle it would be possible to use the same concept for H_2O_2 visualization, the complex electronic structure of H_2O_2 makes it challenging [71]. It might, however, be possible to vibrationally excite H_2O_2 by a laser pulse that is intensity modulated and in a second step photodissociate the vibrationally excited H_2O_2 into two OH fragments. A probe pulse could then monitor the intensity modulated OH fragments. As a further development of the technique, the two species may be simultaneously imaged if their intensity modulation varies and thereby the coded OH fragments end up at different locations in the Fourier plane. In such a configuration two different intensity modulated IR-pulses excites either HO_2 or H_2O_2, whereupon the same pump pulse dissociates the species into OH and O fragments. The OH fragments, having different modulation frequency depending on origin, can then be imaged by a probe pulse and the desired signals extracted in the post processing. Simultaneous single-shot imaging of both HO_2 and H_2O_2 may then be performed in turbulent environments.

Acknowledgments

I have met and collaborated with many people since I started my PhD in 2012, all of whom I would like to acknowledge for contributing to this work. However, all of you may not be mentioned by name here, still your support is highly appreciated.

I would like to start by thanking my supervisor *Joakim Bood* for the great support you have given me during these years including but not limited to, lab activities, writing support and data evaluation. In particular, I appreciate your ability to always dig into details when it comes to physics or chemistry. As a researcher, you have and will be a big inspiration for me in my future career. I also value the many non-work related discussions we have had during my PhD. It is always fun and easy to talk to you no matter the topic.

I would also like to thank my co-supervisor *Marcus Aldén* for your valuable input to this thesis and the papers it includes. It always impresses me each time you remember details regarding a paper you published 20 years ago and find the relevant documents immediately.

Throughout these years, I have had the opportunity to work closely with many people such as *Malin Jonsson*, *Olof Johansson*, *Jesper Borggren*, *Dina Hot*, *Andreas Ehn*, *Andreas Lantz*, *Elias Kristensson*, *Jinlong Gao*, *Chengdong Kong* and *Wubin Weng*. The two intensive months Olof and I spent together in the lab at the start of my PhD work really improved my abilities as a researcher. Malin and Jesper you have enlivened countless of hours in the lab, especially when we have been struggling with the pico-laser. Further, I will never forget the time Dina and I spent on fixing the Excimer laser and aligning it over and over again. Andreas, I admire your passion about science and your ability of always finding ways to make research appear easy. I really appreciate that you always have had the time for my many questions.

Although, we never really worked together *Elin Malmqvist* and I have shared an office for almost my entire PhD study, which has been the start of a beautiful friendship. It has always been a great pleasure and the days at the division are just a lot better when you are around. I have especially, appreciated our trips together and the many internal jokes about "mannen med mustachen". Also, I really value the power-point countdown you made for me, it has made me smile every morning. *Johan Simonsson*, I would like to thank you for sharing your daily agenda with me and I appreciate your way of always knowing what is right or wrong.

I would also like to take the opportunity to thank *Vladimir Alekseev* for simulating the data needed to produce the branching ratios in Figure 4.3.3. I always appreciated

your Tuesday presentations, where you apply your research to "real" things such as films.

I am very happy that *Jim Larsson*, *Maria Ruchkina* and *Pengji Ding* are part of our research group you are all very fun to be around. Jim, I appreciate our discussions and I want to "thank you for nothing".

Thank you *Christian Brackmann* for always helping me whether it is MATLAB or alignement of the dye laser. I value your input as well as your many stories. I will also like to acknowledge *Minna Ramkull*, *Cecilia Bille* and *Igor Buzuk* for your administrative as well as technical support. Especially, I would like to thank Minna for making the division such a nice working place. Your "knake fika" and gingerbread baking is just a few of the wonderful things you do for the division.

My days at Combustion physics would not be the same without all the people working there. In particular, I would like to mention *Per-Erik Bengtsson*, *Sven-Inge Möller*, *Edouard Berrocal*, *Arman Ahmed Subash*, *Anna-lena Sahlberg*, *Panagiota Stamatoglou*, *Sandra Török*, *Ali Hosseinnia*, *Moah Christensen*, *Joakim Jönsson*, *Samuel Jansson* and *Fahed Abou Nada* for making the division such a nice place.

Alaa Omrane, *Hans Seyfried* and *Ulf Lindblad* at Tetra Pak are also acknowledged for technical assistance during the measurement campaign at Tetra Pak as well as interesting and fun discussions. A special thanks to Alaa for having me as a master student and inspiring me to start this PhD study.

I would like to thank the Centre for Combustion Science and Technology, CECOST, for the financial support.

Last but not least, I would like to thank my family and friends for supporting me during these years. Especially, my dad, for listening to my complaints but yet supporting me in all my decisions, and my parents-in-law for letting me be a part of the Garting family despite my surname. Thank you Tommy for always supporting me, you are the love of my life, my best friend and you have given me the best of gifts, our little miracle Alicia.

References

1. Johansson O, Bood J, Li B, Ehn A, Li ZS, Sun ZW, Jonsson M, Konnov AA, Aldén M. "*Photofragmentation laser-induced fluorescence imaging in premixed flames.*" Combust Flame. 2011;158(10):1908–1919.

2. Li B, Zhang D, Yao M, Li Z. "*Strategy for single-shot CH_3 imaging in premixed methane/air flames using photofragmentation laser-induced fluorescence.*" Proc Combust Inst. 2017;36(3):4487–4495.

3. Li B, Jonsson M, Algotsson M, Bood J, Li ZS, Johansson O, Aldén M, Tunér M, Johansson B. "*Quantitative detection of hydrogen peroxide in an HCCI engine using photofragmentation laser-induced fluorescence.*" Proc Combust Inst. 2013;34(2):3573–3581.

4. Osborn DL, Frank JH. "*Laser-induced fragmentation fluorescence detection of the vinyl radical and acetylene.*" Chem Phys Lett. 2001;349(1–2):43–50.

5. Aldén M, Bood J, Li Z, Richter M. "*Visualization and understanding of combustion processes using spatially and temporally resolved laser diagnostic techniques.*" Proc Combust Inst. 2011;33(1):69–97.

6. Kohse-Höinghaus K. "*Laser techniques for the quantitative detection of reactive intermediates in combustion systems.*" Prog Energy Combust Sci. 1994;20(3):203–279.

7. Daily JW. "*Laser induced fluorescence spectroscopy in flames.*" Prog Energy Combust Sci. 1997;23(2):133–199.

8. Robertson GL. "*Food Packaging: Principles and Practice.*" Vol. 32, IFLA Journal. 2006. 179-180 p.

9. Ansari IA, Datta AK. "*An Overview of Sterilization Methods for Packaging Materials Used in Aseptic Packaging Systems.*" Food Bioprod Process. 2003;81(1):57–65.

10. Laroussi M. "*Sterilization of contaminated matter with an atmospheric pressure plasma.*" IEEE Trans Plasma Sci. 1996;24(3):1188–1191.

11. Adams D, Brown GP, Fritz C, Todd TR. "*Calibration of a near-infrared (NIR) H_2O_2 vapor monitor.*" Pharm Eng. 1998;18(3):1–11.

12. Slemr F, Harris G., Hastif D., Mackay G., Schiff H. "*Measurement of gas phase hydrogen peroxide in air by tunable diode laser absorption spectroscopy.*" J Geophys Res. 1986;91(D5):5371–5378.

13. Corveleyn S, Vandenbossche GMR, Remon JP. "*Near-Infrared (NIR) Monitoring of H_2O_2 Vapor Concentration During Vapor Hydrogen Peroxide (VHP) Sterilisation.*" Pharm Res. 1997;14(3):294–298.

14. Hagen CL, Sanders ST. "*Investigation of multi-species (H_2O_2 and H_2O) sensing and thermometry in an HCCI engine by wavelength-agile absorption spectroscopy.*" Meas Sci Technol. 2007;18(7):1992–1998.

15. Laroussi M. "*Low temperature plasma-based sterilization: Overview and state-of-the-art.*" Plasma Process Polym. 2005;2(5):391–400.

16. Ju Y, Sun W. "*Plasma assisted combustion: Dynamics and chemistry.*" Prog Energy Combust Sci. 2015;48(C):21–83.

17. Zhu J, Ehn A, Gao J, Kong C, Aldén M, Salewski M, Leipold F, Kusano Y, Li Z. "*Translational, rotational, vibrational and electron temperatures of a gliding arc discharge.*" Opt Express. 2017;25(17):3343–3351.

18. Zhu J. "*Optical Diagnostics of Non-thermal Plasmas and Plasma-assisted Combustion.*", PhD Thesis, Lund University. 2015.

19. Ombrello T, Qin X, Ju Y, Gutsol A, Fridman A, Carter C. "*Combustion Enhancement via Stabilized Piecewise Nonequilibrium Gliding Arc Plasma Discharge.*" AIAA J. 2006;44(1):142–150.

20. Eckbreth AC. "*Laser diagnostics for combustion temperature and species.*" Vol. 3. CRC Press; 1996.

21. Rodgers MO, Asai K, Davis DD. "*Photofragmentation-laser induced fluorescence: a new method for detecting atmospheric trace gases.*" Appl Opt. 1980;19(21):3597–3605.

22. Davis DD, Heaps WS, Philen D, Rodgers M, McGee T, Nelson A, Moriarty AJ. "*Airborne laser induced fluorescence system for measuring OH and other trace gases in the parts-per-quadrillion to parts-per-trillion range.*" Rev Sci Instrum. 1979;50(12):1505–1516.

23. DeMore WB, Sander SP, Golden DM, Hampson RF, Kurylo MJ, Howard CJ, Ravishankara AR, Kolb CE, Molina MJ. "*Chemical kinetics and photochemical data for use in stratospheric modeling.*" JPL Publ. 1997;4(12):278.

24. Atkinson R, Baulch DL, Cox R, Crowley JN, Hampson RF, Hynes RG, Jenkin ME, Rossi MJ, Troe J. "*Evaluated kinetic and photochemical data for atmospheric chemistry: Part 1 - gas phase reactions of O_x, HO_x, NO_x and SO_x species.*" Atmos Chem Phys Discuss. 2003;3(6):6179–6699.

25. Andresen P, Bath A, Gröger W, Lülf HW, Meijer G, Meulen JJ. "*Laser-induced fluorescence with tunable excimer lasers as a possible method for instantaneous temperature field measurements at high pressures: checks with an atmospheric flame.*" Appl Opt. 1988;27(2):365–378.

26. Grinstead JH, Laufer G, J.C. McDaniel J. "*Single-pulse, two-line temperature-measurment technique using KrF laser-induced O_2 fluorescence.*" Appl Opt. 1995;34(24):5501–5512.

27. Lin CL, Rohatgi NK, DeMore WB. "*Ultraviolet absorption cross sections of hydrogen peroxide.*" Geophys Res Lett. 1978;5(2):113–115.

28. Luque J, Crosley D. "*LIFBASE: Database and Spectral Simulation Program.*" SRI International Report MP 99-009; 1999.

29. Matsumi Y, Kawasaki M. "*Photolysis of Atmospheric Ozone in the Ultraviolet Region.*" Chem Rev. 2003;103(12):4767–4781.

30. Park H, Slanger TG. "*$O_2(X,v=8–22)$ 300 K quenching rate coefficients for O_2 and N_2, and $O_2(x)$ vibrational distribution from 248 nm O_3 photodissociation.*" J Chem Phys. 1994;100(1):287.

31. Geiser J, Dylewski SM, Mueller J a, Wilson RJ, Toumi R, Houston PL. "*The vibrational distribution of $O_2(X^3\Sigma_g^-)$ produced in the photodissociation of ozone between 226 and 240 and at 266 nm.*" J Chem Phys. 2000;112(3):1279–1286.

32. Finlayson-Pitts BJ, Pitts Jr. JN. "*CHAPTER 4 - Photochemistry of Important Atmospheric Species BT - Chemistry of the Upper and Lower Atmosphere.*" In San Diego: Academic Press; 2000. p. 86–129.

33. Vaghjiani GL, Turnipseed A, Warren RF, Ravishankara R. "*Photodissociation of H_2O_2 at 193 and 222 nm: Products and quantum yields.*" J Chem Phys. 1992;96(8):5878.

34. Vaghjiani GL, Ravishankara AR. "*Photodissociation of H_2O_2 and CH_3OOH at 248 nm and 298 K: Quantum yields for OH, $O(^3P)$ and $H(^2S)$.*" J Chem Phys. 1990;92(2):996–1003.

35. Ondrey G. "*The state distribution of OH radicals photodissociated from H_2O_2 at 193 and 248 nm.*" J Chem Phys. 1983;78(6):3732.

36. Cai ZT, Zhang DH, Zhang JZH. "*Quantum dynamical studies for photodissociation of H_2O_2 at 248 and 266 nm.*" J Chem Phys. 1994;100(January):5631–5638.

37. Vazquez GJ, Peyerimhoff SD, Buenker RJ. "*MRD CI study of the photodissociation of HO_2 into $OH(X^2II)$ + $O(^3P, {}^1D)$.*" Chem Phys. 1985 Oct;99(2):239–257.

38. Lee LC. "*Observation of $O(^1D)$ produced from photodissociation of HO_2 at 193 and 248 nm.*" J Chem Phys. 1982;76(10):4909–4915.

39. Sinha A, Coleman J, Barnes R. "*Photodissociation Dynamics of HO_2 at 220 nm: Determination of the $O(^1D):O(^3P)$ Branching Ratio.*" J Phys Chem. 1994;98:12462–12465.

40. Hynes AJ, Richter RC, Nien CJ. "*Laser photofragmention-laser induced fluorescence detection of the hydroperoxyl radical: Photofragment energy distributions, detection sensitivity and kinetics.*" Chem Phys Lett. 1996;258(5–6):633–638.

41. Hogan P, Davis DD. "*Electronic quenching and vibrational relaxation of the OH (A $^2\Sigma^+$, v'=1) state.*" J Chem Phys. 1975;62(11):4574–4576.

42. Neil M, Juskaitis R, Wilson T. "*Method of obtaining optical sectioning by using structured light in a conventional microscope.*" Opt Lett. 1997;22(24):1905–1907.

43. Kristensson E, Ehn A, Kristensson E, Ehn A, Bood J, Aldén M. "*Advancements in Rayleigh Scattering Thermometry by Means of Structured Illumination.*" Proc Combust Inst. 2015;35(June):3689–3696.

44. Kristensson E. "*Structured laser illumination planar imaging SLIPI applications for spray diagnostics.*", PhD Thesis, Lund University; 2012.

45. Jonsson M. "*Short-Pulse Photofragmentation and Fluorescence-based Diagnostics-Development and Applications.*", PhD Thesis, Lund University; 2015.

46. Hutchinson IH. "*Principles of Plasma Diagnostics.*", PhD Thesis, Cambridge University Press; 2005.

47. Lee DH, Kim KT, Cha MS, Song YH. "*Optimization scheme of a rotating gliding arc reactor for partial oxidation of methane.*" Proc Combust Inst. 2007;31 II:3343–3351.

48. Michael JB. "*Localized microwave pulsed plasmas for ignition and flame front enhancement.*", PhD Thesis, Princeton University; 2012.

49. Rusterholtz D. "*Nanosecond repetitively pulsed discharges in atmospheric pressure air.*" Ecole Centrale Paris; 2012.

50. Ono R. "*Optical diagnostics of reactive species in atmospheric-pressure nonthermal plasma.*" J Phys D Appl Phys. 2016;49(8):83001.

51. Zhao T-L, Xu Y, Song Y-H, Li X-S, Liu J-L, Liu J-B, Zhu A-M. "*Determination of vibrational and rotational temperatures in a gliding arc discharge by using overlapped molecular emission spectra.*" J Phys D Appl Phys. 2013;46(34):345201.

52. Tochikubo F, Teich TH. "*Optical emission from a pulsed corona discharge and its associated reactions.*" Japanese J Appl Physics, Part 1 Regul Pap Short Notes Rev Pap. 2000;39(3 A):1343–1350.

53. Fridman. "*Rotational, vibrational, and excitation temperatures of a microwave-frequency microplasma.*" IEEE Trans Plasma Sci. 2004;32(2):498–504.

54. Sankaranarayanan R, Pashaie B, Dhali SK. "*Laser-induced fluorescence of OH radicals in a dielectric barrier discharge.*" Appl Phys Lett. 2000;77(19):2970–2972.

55. Mazouffre S, Foissac C, Supiot P, Vankan P, Engeln R, Schram DC, Sadeghi N. "*Density and temperature of N atoms in the afterglow of a microwave discharge measured by a two-photon laser-induced fluorescence technique.*" Plasma Sources Sci Technol. 2001;10:168–175.

56. Muraoka K, Uchino K, Yamagata Y, Noguchi Y, Mansour M, Suanpoot P, Narishige S, Noguchi M. "*Laser Thomson scattering studies of glow discharge plasmas.*" Plasma Sources Sci Technol. 2002;11(3A):A143.

57. Pitz RW, Brown TM, Nandula SP, Skaggs P, Debarber P, Brown MS, Segall J. "*Unseeded velocity measurement by ozone tagging velocimetry.*" Opt Lett. 1996;21(10):755–757.

58. Dogariu A, Shneider MN, Miles RB. "*Versatile radar measurement of the electron loss rate in air.*" Appl Phys Lett. 2013;103(22).

59. Terrell C, Hansen DL, Ajello JM. "*The near-ultraviolet and visible emission spectrum of O_2 by electron impact.*" J Phys B At Mol Opt Phys. 2004;37(9):1931–1949.

60. Wang ZH, Li B, Ehn A, Sun ZW, Li ZS, Bood J, Aldén M, Cen KF. "*Investigation of flue-gas treatment with O_3 injection using NO and NO_2 planar laser-induced fluorescence.*" Fuel. 2010;89(9):2346–2352.

61. Sun ZW, Zhu JJ, Li ZS, Aldén M, Leipold F, Salewski M, Kusano Y. "*Optical diagnostics of a gliding arc.*" Opt Express. 2013;21(5):6028–6044.

62. Kanazawa S, Sumi T, Sato N, Ohkubo T, Nomoto Y, Kocik M, Mizeraczyk J, Chang JS. "*Wide-range two-dimensional imaging of NO density profiles by LIF technique in a corona radical shower reactor.*" IEEE Trans Ind Appl. 2005;41(1):200–205.

63. Bowden MD, Goto Y, Yanaga H, Howarth PJA, Uchino K, Muraoka K. "*Thomson scattering diagnostic system for measurement of electron properties of processing plasmas.*" Plasma Sources Sci Technol. 1999;8(2):203–209.

64. Sheffield J, Froula D, Glenzer SH, Luhmann Jr NC. "*Plasma scattering of electromagnetic radiation: theory and measurement techniques.*" Academic press; 2010.

65. Muraoka K, Uchino K, Bowden MD. "*Diagnostics of low-density glow discharge plasmas using Thomson scattering.*" 1998;40:1221–1239.

66. Fink EH, Ramsay D a. "*High-Resolution Study of the A^2A' -> X^2A'' Transition of HO_2: Analysis of the 000 – 000 Band.*" J Mol Spectrosc. 1997;185(185):304–324.

67. Hunziker HE, Wendt HR. "*Near infrared absorption spectrum of HO_2.*" J Chem Phys. 1974;60(11):4622–4623.

68. Becker KH, Fink EH, Langen P, Schurath U. "*Near infrared emission bands of the HO_2 radical.*" J Chem Phys. 1974;60(11):4623.

69. Tuckett RP, Freedman PA, Jones WJ. "*The emission bands of HO_2 between 1.43 and 1.51 μm.*" Mol Phys. 1979;37(2):379–401.

70. Jensen RJ, Guettler RD, Lyman JL. "*The ultraviolet absorption spectrum of hot carbon dioxide.*" Chem Phys Lett. 1997;277(4):356–360.

71. Gericke K, Klee S, Comes FJ, Dixon RN. "*Dynamics of H_2O_2 photodissociation: OH product state and momentum distribution characterized by sub-Doppler and polarization spectroscopy.*" J Chem Phys. 1986;85(8):4463.

Summary of papers

I. In this paper simultaneous visualization of hydrogen peroxide and water vapor are demonstrated. Water vapor is detected via two-photon laser induced fluorescence by a 248 nm laser pulse via the predissociative vibrationless C^1B_1 state, resulting in a featureless fluorescence spectra between 400- and 500 nm upon relaxation to the ground state. Detection of hydrogen peroxide is carried out from photofragmentation laser-induced fluorescence, where a pump pulse (248 nm) photolysis the hydrogen peroxide molecule into two OH radicals and a probe pulse, tuned in to an absorption line of OH (283 nm) excites the OH radicals whom after relaxation emits fluorescence (305-320 nm). Any potential interfering OH fluorescence stemming from the repulsive B^1A_1 state of water was found to be negligible, for most practical applications, compared to the strong OH fluorescence originating from hydrogen peroxide.

I planed the experiment together with Olof Johansson and Joakim Bood. Olof and I carried out the experiments, while I did most of the data analysis. Joakim wrote the manuscript.

II. Simultaneous visualization of H_2O_2 and H_2O was presented in this paper using the characteristics of OH emission stemming from photolysis of hydrogen peroxide. The total OH emission reflects the H_2O_2 concentration, while the ratio between the OH emission bands gives the water vapor concentration. The concept is based on that quenching from water molecules affects the intensity distribution of OH emission originating from H_2O_2 photolysis and thereby requires that the probe volume is in a bath gas that has low cross section for collisional quenching and *VET*.

Joakim Bood and I planed the experiment together. I was responsible for the experimental work and analyzed the data. Joakim developed the model and we wrote the manuscript together.

III. Picosecond laser pulses were used to investigate the chemical build-up of OH in the reaction- and product zone upon photolysis of hydrogen

peroxides in a stoichiometric laminar CH_4/air flame. A chemical model for the OH production was developed and compared with experimental data. In addition, the intensity of OH signal stemming from CO_2 photochemistry could be minimized since the pump-probe delay time was a couple of nanoseconds.

I mainly took part in the experimental work together with Malin Jonsson and Jesper Borggren. The chemical model was developed by Joakim Bood, whom wrote the manuscript with Malin.

IV. This manuscript presents a concept based on PFLIF and structured illumination for instantaneous imaging of hydrogen peroxides in flames. The pump beam has a spatially intensity modulated pattern, and thereby giving the formed OH fragments a recognizable pattern. The OH fragments, stemming from hydrogen peroxides, can then be extracted by a post-processing routine by turning the recorded PFLIF image to the frequency domain.

Me, Malin Jonsson and Jesper Borggren planned and conducted the experiments. We also performed the data analysis together with Andreas Ehn and Elias Kristensson. All authors contributed on writing the manuscript.

V. Imaging of ozone was conducted in a slightly turbulent ozone flow by using PFLIF with a laser pulse at 248 nm. The laser pulse thereby acted as both photolysis and probe pulse. A detailed study of emission- and excitation wavelengths were performed as well as simultaneous spectroscopic- and imaging measurements under combustion like conditions.

I took part in planning and conducting the experimental work and contributed to most of the data analysis. Me, Dina Hot, Andreas Ehn and Joakim Bood wrote the manuscript together.

VI. In this paper, ozone was imaged in a plasma produced by a gliding arc discharge using PFLIF with a 248 nm laser pulse. An additional laser pulse at 266 nm was introduced as pump pulse to separate the pump- from the probe processes in order to study the lifetime of vibrationally hot O_2 in both a laminar O_3 flow and a plasma produced by the gliding arc discharge. The lifetime of O_3, produced by the gliding arc discharge, was also investigated and it was found that the lifetime of O_3 was several orders of magnitude longer than the lifetime of hot O_2. It was concluded that

ozone could be monitored in the plasma produced by the gliding arc discharge if the discharge was turned off several microseconds prior to the arrival of the pump pulse. Nevertheless, a calculation estimated that the number of naturally present hot O_2, produced by the gliding arc discharge (0.8 eV), was minor compared to the amount of hot O_2 formed from photolysis of O_3 and hence ozone could be visualized in the plasma when the discharge was operating.

Me and Dina Hot was responsible for planning and conducting the experimental work regarding the laser beams, while Jinlong Gao, Chengdong Kong and Andreas Ehn was responsible for operating the gliding arc discharge setup. The manuscript was mainly written by me and Andreas.

VII.   Quantitative NO_2 measurements using LIF were carried out in a plasma produced by electron beam in a sterilization rig at Tetra Pak. Highly energetic electrons were accelerated through a vacuum pipe and a plasma was created as the electrons interacted with ambient air. The NO_2 concentration was determined for various settings in the rig and the results were used to, as a first approximation, estimate the O_3 concentration in the plasma.

Joakim Bood and I planned the experiments together with Hans Seyfried. I conducted most of the experimental work and analyzed all the data. The manuscript was written by me and Joakim.

LUND
UNIVERSITY